

Fabrication, Properties and Applications of all- inorganic lead halide nanostructures

KATERINA ARGYROU

Department of Material Science and Technology

Heraklion 2019

To my mother Maria
and my grandfather Kostas

Acknowledgments

I would first like to express my sincere gratitude to my research supervisor, Dr Emmanuel Stratakis for his trust and all the learning opportunities during this project. I am also grateful for the large freedom to work in the lab and the consistence encouragement he provided.

I would like to thank the rest of my thesis committee, Prof. George Kioseoglou and Prof. Maria Vamvakaki for their support.

The completion of this thesis could not have been accomplished without the support of Dr Athanasia Kostopoulou and Dr Konstantinos Brintakis. I would like to thank them for their precious help, guidance, encouragement and patience till the end of this thesis. I have been highly benefited by this collaboration, gained a lot of knowledge and feel lucky to work under their directions.

I also would like to thank Dr Emmanuel Gagaoudakis for providing an amount of his precious time and effort for me, the Transparent Conductive Materials laboratory for all the needed equipment, Ms Aleka Manousaki for the professional help in SEM/EDS characterizations and Mr Lambros Papoutsakis for the XRD training.

Finally, I would like to thank my family and especially my mother for her support during all those years.

Abstract

Over the past few years all-inorganic lead halide perovskite nanostructures have been intensively studied due to their attractive optical and electronic properties. In general, perovskite materials are sensitive to a variety of environmental factors, however, under certain conditions, reversed changes in perovskite's electrical behavior can be observed, indicating the great potential for sensing applications. For this purpose, well-formed and distorted all-inorganic lead halide nanocubes were fabricated by facile, simple and cost-effective methods and were investigated as ozone and hydrogen sensing elements. In the case of ozone sensing, both materials were self-powered and operated at room temperature. The sensing measurements revealed that they exhibit high sensing ability in a wide range of ozone concentrations, fast response and remarkable repeatability. In particular, the sensitivity of well-formed nanocubes was 54% at 187 ppb while for distorted nanocubes was 13% at 4 ppb, which were the highest reported values among other sensing elements operating at room temperature to date.

Additionally, distorted CsPbBr₃ nanocubes were further investigated as self-powered hydrogen sensing element. The sensor operated at room temperature, exhibited high sensitivity (1.5% at 1 ppm) and fast response and recovery times. Moreover, the unaltered morphology and stoichiometry of the nanocubes after the hydrogen treatment revealed the stability of the sensor. Those promising properties as well as the stability of the sensors after the ozone and hydrogen treatments provide new opportunities in gas sensing technology.

TABLE OF CONTENTS

Acknowledgments	4
Abstract	5
CHAPTER 1: INTRODUCTION	8
1.1 Nanoparticles (NPs)	8
1.2 An overview of perovskites	9
1.3 Synthesis of perovskite nanocrystals	13
1.4 Motivation	14
CHAPTER 2: MATERIAL DEVELOPMENT AND CHARACTERIZATION TECHNIQUES	16
2.1 Materials fabrication	16
2.1.1 Room temperature synthesis of well-formed CsPbBr ₃ nanocrystals in Ar atmosphere	16
2.1.2 Room temperature synthesis of distorted CsPbBr ₃ nanocrystals under ambient conditions	16
2.2 Characterization techniques	17
2.2.1 Scanning Electron Microscopy (SEM)/ Energy Dispersive Spectroscopy (EDS)	17
2.2.2 Ultraviolet – visible spectroscopy (UV/Vis)	18
2.2.3 X-Ray Diffraction (XRD)	22
2.3 Gas sensing experimental set up	23
CHAPTER 3: MORPHOLOGY, STRUCTURE AND OPTICAL PROPERTIES	25
3.1 Reaction procedure and nanocrystal formation	25
3.2 Structure Determination of the perovskite nanocubes	26
3.3 Optical properties of the CsPbBr ₃ nanocubes	30
CHAPTER 4: ALL-INORGANIC LEAD HALIDE NANOCUBES AS GAS SENSORS	32
4.1 Perovskite nanocubes sensors	32

4.2 CsPbBr ₃ Nanocubes for ozone gas sensing	33
4.3 Sensing Mechanism	50
4.4 CsPbBr ₃ Nanocubes for hydrogen gas sensing	51
4.5 Sensing mechanism	57
CHAPTER 5: CONCLUSIONS	59
References	60

CHAPTER 1: INTRODUCTION

1.1 Nanoparticles (NPs)

The term nanoparticle refers to a wide class of materials that include particulate substances with at least one dimension less than 100 nm. Nanoparticles (NPs) have been intensively studied as they exhibit size-dependent optical, electronic and magnetic properties that differ from the corresponding bulk materials.¹ Quantum confinement in semiconductor NPs, surface plasmon resonance in some metal NPs and supermagnetism in magnetic particles are just few of the properties that can be modified by changing the size, shape, surface and inner structure of NPs.^{2,3}

NPs can be naturally found in the atmosphere, in natural waters and soils or can be artificially synthesized. Based on their structure, NPs can be classified either as amorphous or crystalline, also known as nanocrystals (NCs), and depending on the synthetic method, they can be produced in various geometric shapes and structures (Figure 1.1).⁴

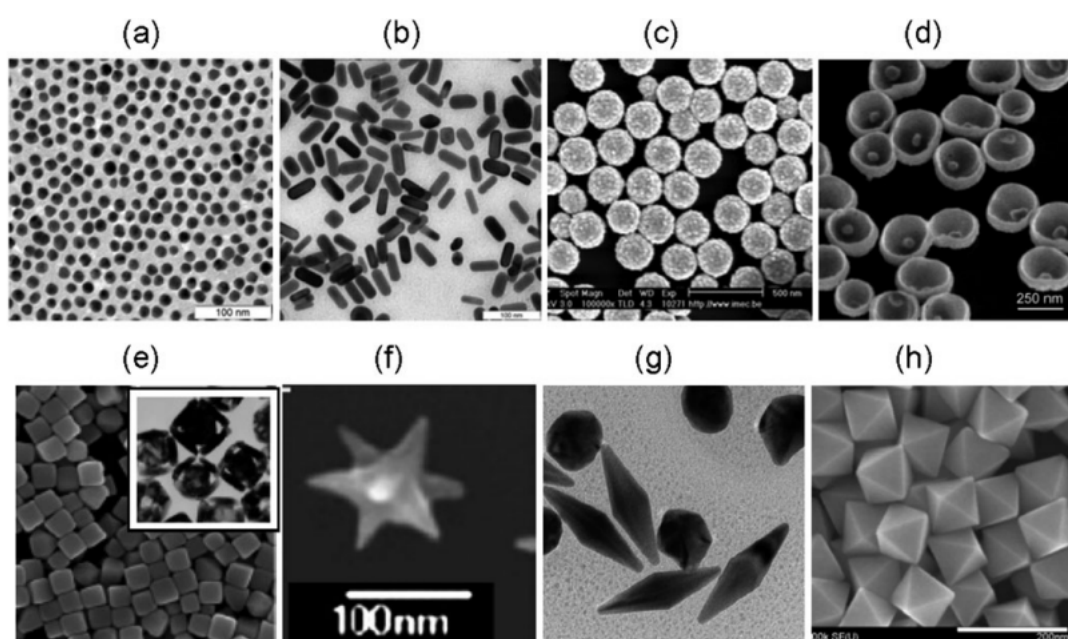


Figure 1.1 Different shapes of NPs. Nanospheres (a), nanorods (b), nanoshells (c), nanobowls (d), nanocubes and nanocages (insert) (e), nanostars (f), bipyramids (g) and octahedral (h).⁵

Considering the unique properties of NPs in combination with the appropriate size scale, nano-sized materials can be used in a wide range of industrial and commercial applications. Those practical applications are related with a variety of areas ranging from environment, such as the detection of air pollutant gases, to other fields including chemistry, engineering and physics (Figure 1.2).⁶

In the biomedical field, NPs have also gained great attention due to their ability to deliver drugs in the optimum dosage range and increase therapeutic efficiency, while they minimize side effects and improve patient compliance.⁷ In addition, based on their optical properties, NPs have been used for biological and cell imaging and photo-therapeutic applications.⁸

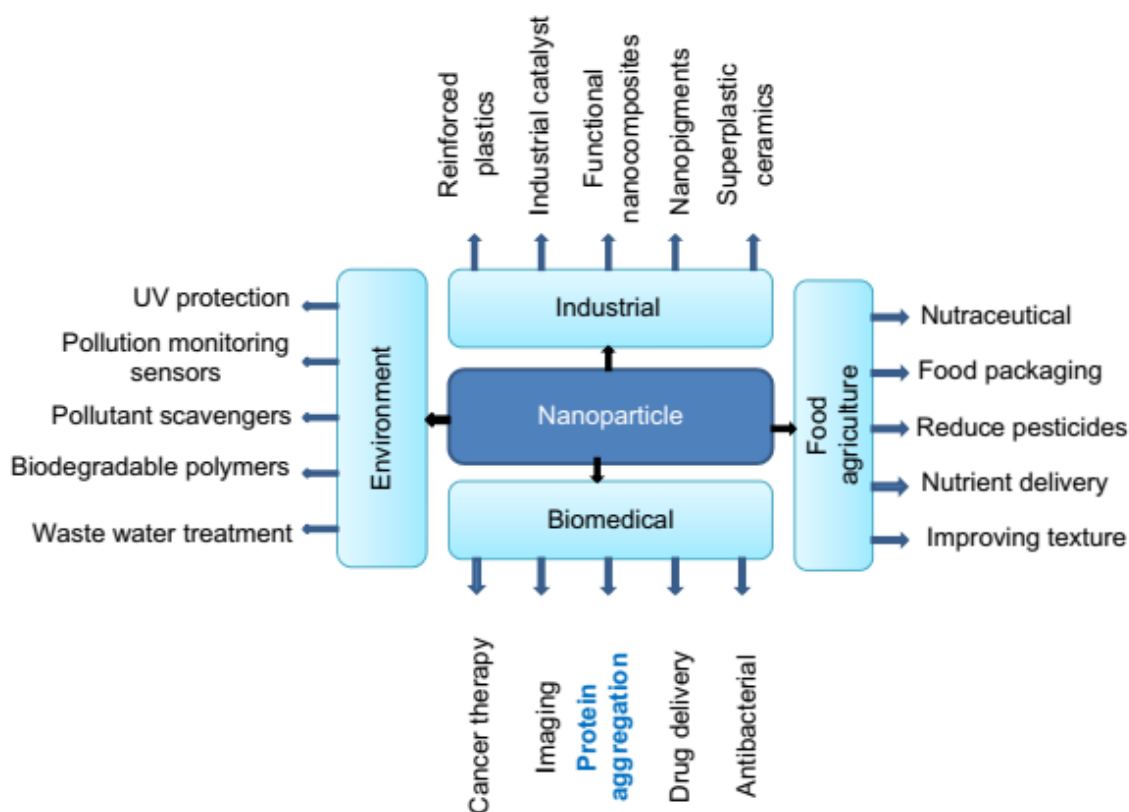


Figure 1.2 Applications of NPs in various fields. ⁶

1.2 An overview of perovskites

In recent years, perovskite nanostructures have emerged as very promising and efficient materials for various optoelectronic applications. Perovskite is the naturally occurring mineral of calcium titanate with a chemical formula of CaTiO_3 . This mineral was named after the Russian mineralogist Lev Perovski.⁹ In general, perovskite materials are considered the materials with the same crystal structure as CaTiO_3 . The general chemical formula of perovskite materials is ABX_3 , where 'A' and 'B' are two cations of very different sizes and 'X' is an anion, usually oxide or halogen.¹⁰

Recently, nano-sized metal halide perovskites have attracted significant attention due to their unique optical and electronic properties, including band gap tunability, bright emission with high photoluminescence quantum yield (PLQY) and high charge carrier mobility. Benefiting from those properties, metal halide perovskites nanostructures

are regarded as next generation candidates for applications in solar cells,¹¹ light emitting diodes (LEDs),¹² lasers¹³ and photodetectors¹⁴.

Regarding metal halide perovskites, cation 'A' is an organic molecule, usually methylammonium (MA) or formamidinium (FA), or an alkali metal, commonly Cs, 'B' is a divalent metal cation such as Pb, Ge or Sn and 'X' is a monovalent halide anion (Cl, I or Br). The three dimensional (3D) crystal structure of metal halide perovskites is characterized by corner-sharing $[BX_6]^{4-}$ octahedra, with the A cations located in the voids between those octahedra, resulting a cubic structure (Figure 1.3a). However, the ideal cubic perovskite structure is not as common as the orthorhombic structure which differs from the idealized cubic structure by an octahedral tilting (Figure 1.3b).^{15, 16}

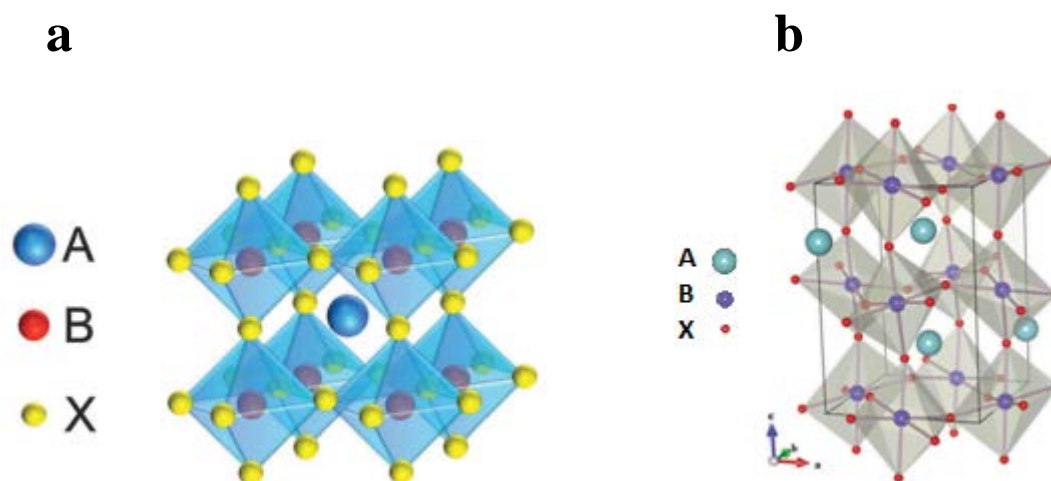


Figure 1.3 Schematic representation of ABX_3 perovskite cubic (a) and orthorhombic (b) structure.^{15, 17}

Lowering the dimensional structure of perovskites, a number of optical properties can be manipulated. As a consequence, low dimensional perovskite-related structures, with the chemical formula A_nBX_{2+n} , have been intensively studied. Among these compounds, $CsPb_2X_5$ is being looked up broadly for potential applications in optoelectronic.¹⁸ $CsPb_2Br_5$ NCs present a two-dimensional (2D) structure which consists of Cs^+ and $[Pb_2X_5]^-$ alternating layers. In the $[Pb_2X_5]^-$ layer, one Pb^{2+} coordinates with four X anions, forming an elongated pentahedron (Figure 1.4).¹⁹ To date, the morphological dimensionality of perovskites has been further controlled and even lower-dimension perovskites have been developed and studied (Figure 1.5).²⁰

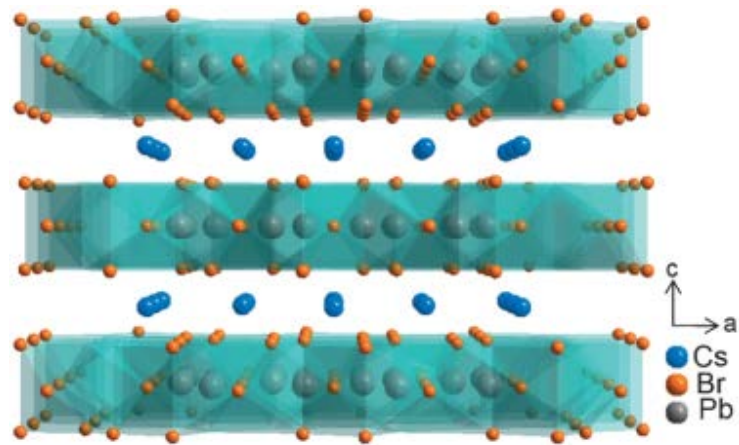


Figure 1.4 Perovskite – related crystal structure of CsPb_2Br_5 .¹⁹

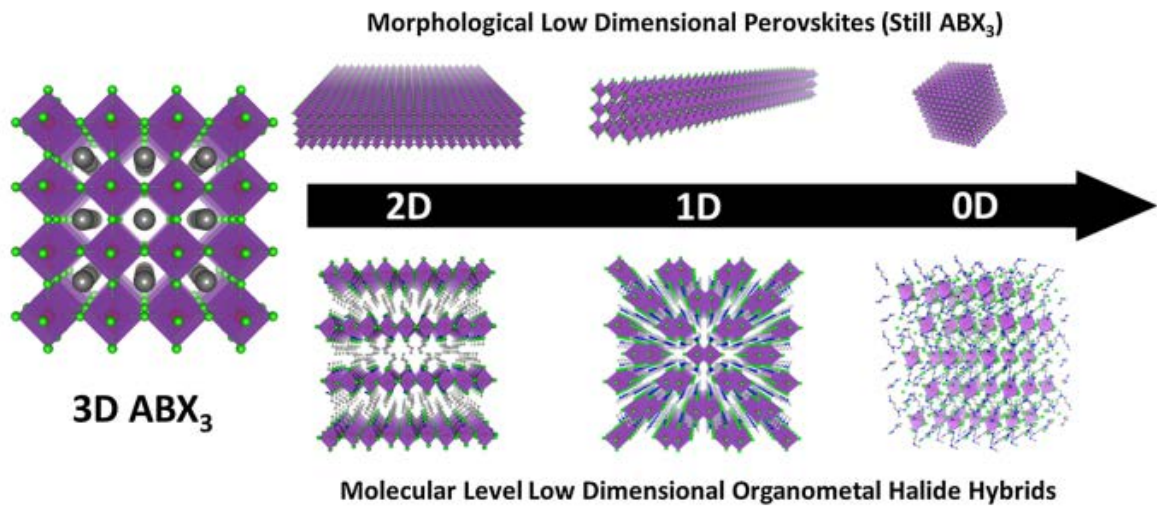


Figure 1.5 Three-dimensional metal halide perovskites and perovskite-related materials with different dimensionalities at both morphological and molecular level.²⁰

Hybrid organic-inorganic perovskites are currently one of the most attractive fields of research due to their rapid evolution in photovoltaics. The power conversion efficiencies (PCE) of perovskite solar cells have increased from 10% to over 22% within only several years. In striking contrast, silicon – based technologies, which have been successfully commercialized with PCE over 25%, have been developing in more than 40 years (Figure 1.6).²¹

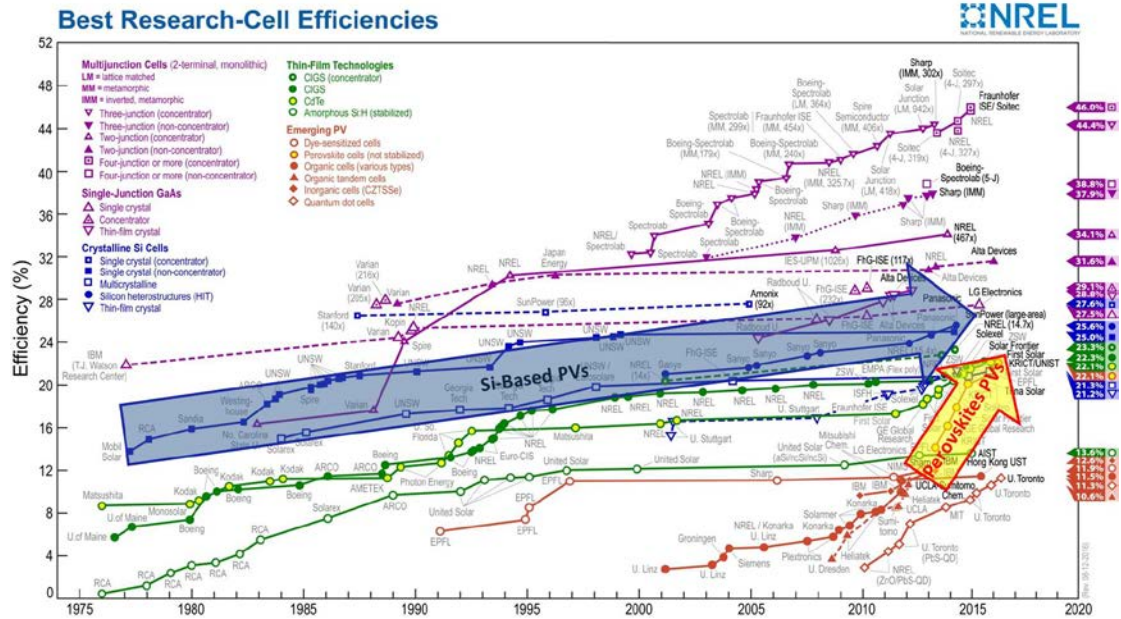


Figure 1.6 Perovskite solar cells evolution (yellow arrow) versus silicon-based solar cells (blue arrow).²¹

Despite the success of hybrid organic–inorganic metal halide perovskite materials in such applications, their sensitivity to factors, such as moisture and oxygen, discourages their further development.²²

Notably, the stability of perovskites can be evaluated by a tolerance factor (t), which is based on the chemical formula ABX_3 and the ionic radii (r) of the ions:

$$t = \frac{r_A + r_X}{\sqrt{2}(r_B + r_X)} \quad (1.1)$$

Stable cubic perovskite structures are formed when tolerance factor is in the range of 0.9 to approximately 1, while distorted perovskite structures, such as orthorhombic, are formed when tolerance factor is between 0.71 and 0.9. During the last years, great efforts have been made in order to enhance the stability of perovskites by coating them with stable and water-resistant materials or ligands. However, the sensitivity of perovskite materials provides an opportunity to use this drawback in effective sensing applications.²³

Recently, all-inorganic cesium lead halide perovskite, $CsPbX_3$ ($X = I, Br$ and Cl), nanocrystals (NCs) have emerged in perovskites family since they present higher stability compared to their hybrid organic-inorganic counterparts. $CsPbX_3$ NCs have been fabricated in different morphologies and sizes, including nanospheres, nanocubes, nanorods, nanowires and nanoplatelets by altering the synthetic conditions.²⁴ The ability to control the particle size and the halide composition of $CsPbX_3$ ($X = Cl, Br, I$) NCs through small variations in synthetic conditions, results to exceptional properties with the most striking example to be the emission tunability over the entire visible spectral region (Figure 1.7).²⁵

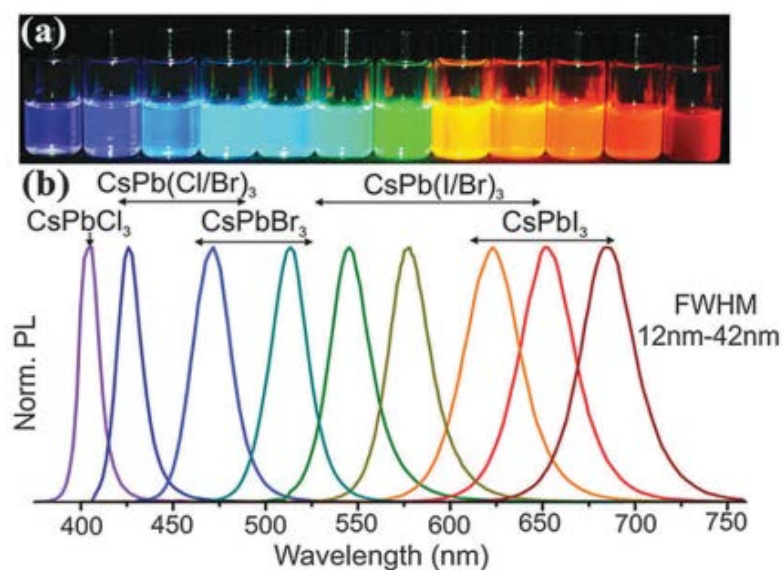


Figure 1.7 Colloidal perovskite CsPbX₃ NCs (X = Cl, Br, I) exhibit size- and composition – tunable bandgap energies covering the entire visible spectral region with narrow and bright emission: (a) colloidal solutions in toluene under UV lamp ($\lambda = 365\text{nm}$), (b) representative PL spectra ($\lambda_{\text{exc}} = 400\text{nm}$, for all but 350 nm for CsPbCl₃ samples).²⁵

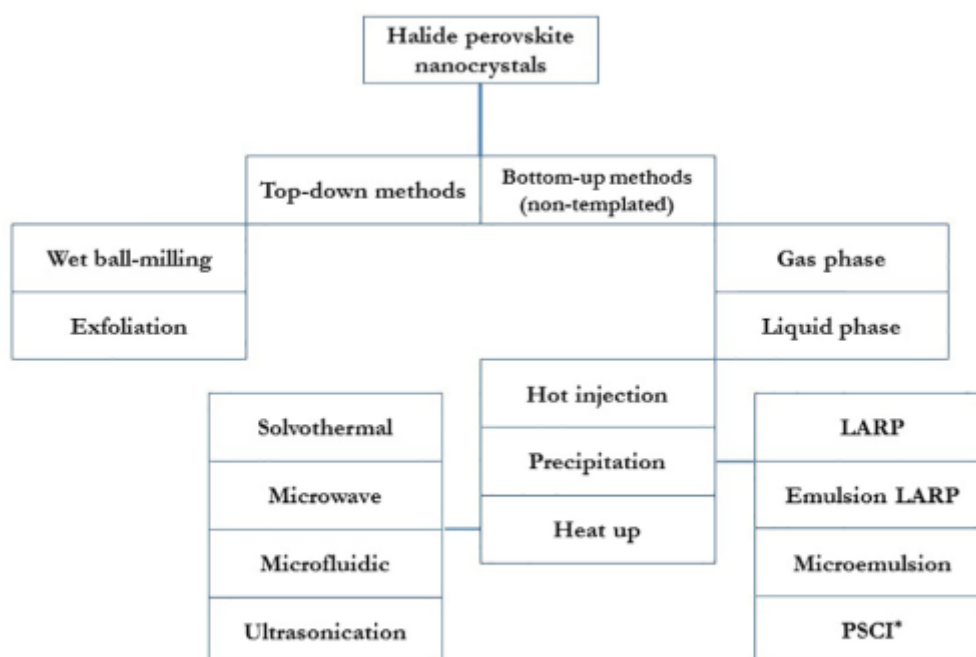
1.3 Synthesis of perovskite nanocrystals

The fabrication methods for high quality metal halide perovskite NCs can be divided into two main categories, ‘top-down’ and ‘bottom-up’ techniques. Top-down methods include the fragmentation and structuring of macroscopic solids, either mechanically or chemically, whereas bottom-up synthetic approaches start from simpler substances and proceed via gas or liquid phase chemical reactions (Figure 1.8).¹ Among all synthetic methods, the most commonly used for the fabrication of well-defined metal halide NCs is the liquid phase approaches, and particularly the hot injection and the precipitation methods.²⁶

The hot injection method is based on the rapid injection of precursor into a hot solution of the remaining precursors, ligands and a high boiling solvent. Hot injection results to an instantaneous nucleation, which terminates by the depletion of monomers. Despite the termination process, the nuclei continue to grow resulting to the formation of defect-free small NCs with a narrow size distribution. The main parameters that allow to control the size and shape of NCs during the synthesis are the reaction medium, the injection temperature, the reaction time and the concentration of the precursor.¹⁶ However, this high temperature process leads to low production of NCs and in order to remove impurities a purification step, such as centrifugation or sonication of NPs, is necessary.²⁷

In order to eliminate the disadvantages of hot injection, a widely used non-injection method has been developed. Re-precipitation process is based on the dissolution of

ions in a solvent and the move of the resultant solution from an equilibrium concentration to a supersaturated state. The supersaturated state can be reached either by cooling the solution, evaporating the solvent or by adding an anti-solvent. Under such conditions, spontaneous precipitation and crystallization reactions take place until the system reaches an equilibrium state again. By this process, the size and shape of NCs can be controlled down to the nanoscale, although, the presence of ligands is required (LARP method). Re-precipitation method is a quick, low-temperature procedure and can provide well crystalline products.²³



*Polar solvent controlled ionization.

Figure 1.8 Methods of synthesis of metal halide perovskite NCs.¹⁶

1.4 Motivation

In order to regulate their morphology, all-inorganic lead halide NCs are often capped by long carbon chain ligands. Such organic ligands create a severe barrier for efficient charge transport, limiting their further efficiency improvement in practical applications. However, the high tolerance of all-inorganic perovskite NCs to environmental factors such as moisture and oxygen makes them tough competitors with other semiconducting materials. Additionally, their ability to change their optical and electronic properties after their exposure to certain conditions has already been reported. The reversibility of those properties in the presence and absence of a wide range of external stimuli allowed perovskite materials to be used for the detection of many factors such as temperature, humidity, a variety of gases, solvents and

explosives. Among all those types of detectors, gas sensors that are able to detect low concentrations of harmful gases are in great demand for either commercial or industrial applications.²³ Hence, the development of cost-effective and ultrasensitive gas sensing elements via simple synthetic approaches is essential.

According to the aforementioned, the scope of this thesis is the fabrication of ligand-free all-inorganic lead halide NCs through a facile and cost effective fabrication process at room temperature for potential gas sensing applications.

CHAPTER 2: MATERIAL DEVELOPMENT AND CHARACTERIZATION TECHNIQUES

2.1 Materials fabrication

2.1.1 Room temperature synthesis of well-formed CsPbBr₃ nanocrystals in Ar atmosphere

CsPbBr₃ NCs were fabricated via a facile room temperature precipitation method. A mixture of 0.4 mmoles of PbBr₂ and 0.4 mmoles of CsBr precursors was dissolved in 10 ml of anhydrous Dimethylformamide (DMF) in a sealed vial closed under Ar in the protective atmosphere of a Glovebox. The mixture was left under mild stirring for two hours. For the formation of CsPbBr₃ nanocubes, 7.6 μ l of the resultant suspension was deposited on commercial InterDigitated platinum electrodes (IDEs, 10 μ m bands/gaps, DropSens) on glass substrate, which will be used for the sensing capability measurements, and before its evaporation, the same amount of anhydrous toluene was added. At this stage, the color of the sample turned into bright yellow, indicating the formation of crystals. The substrate was left to dry for one hour. The entire process took place inside an Ar filled glovebox with O₂ and H₂O concentration below 0.01 ppm.

2.1.2 Room temperature synthesis of distorted CsPbBr₃ nanocrystals under ambient conditions

The precursor solution was prepared in the Glovebox as described in the section 2.1.1 and was removed from it in order to prepare CsPbBr₃ nanocubes directly on the substrate under ambient conditions (Figure 2.1). The procedure was kept exactly the same as previously.



Figure 2.1 Precursors in DMF.

2.2 Characterization techniques

2.2.1 Scanning Electron Microscopy (SEM)/ Energy Dispersive Spectroscopy (EDS)²⁸

A beam of high energy electrons is thermionically emitted from an electron gun usually fitted with a tungsten filament cathode (Figure 2.2a). The electron beam is focused by magnetic lenses at the specimen surface and is scanned across the selected area in a rectangular raster. The interaction of electrons with a sample can result in the generation of many different types of electrons, photons or irradiations (Figure 2.2b). In the case of SEM, secondary electrons (SE) and backscattered electrons (BSE) are collected by detectors and used for imaging while in the case of EDS, characteristic X-rays are used for the elemental analysis (Figure 2.2a). In more details, SE are low energy (10–50 eV) atomic electrons, ejected from the specimen as a result of inelastic scattering. Due to their low energies, SE that are produced at the surface of the specimen are able to escape and be collected by SE detector. Hence, SE are used to image the surface of a specimen. The corresponding signals are measured and the values are mapped as variations in brightness on the image display.

In contrast, the BSE are high-energy incident electrons, elastically scattered with the nuclei of an atom at an angle of 180°. The number of BSE that emerge on the surface of the sample depends on the atomic number. Heavier elements backscatter electrons more strongly than lighter elements, thus they appear brighter in a SEM image. BSE are collected by a solid state semiconductor detector positioned above the sample.

Two types of X-rays are emitted from the interaction of electron beam with a sample, Bremsstrahlung X-rays and characteristic X-rays. Characteristic X-rays are generated by electronic transitions between the electron shells. An electron is ejected from an inner shell of an atom by an electron from the primary beam. Then, an electron from an outer shell fills the inner shell vacancy and an X-ray photon is emitted, with energy equal to the energy difference between the higher and the lower states of the electrons involved in the transition. As each element has specific ionization energies for each energy level, the difference between the energies is characteristic of the element. Hence, characteristic X-rays allow the identification of a sample, while the intensities of the peaks allow the quantitative concentration of the elements.

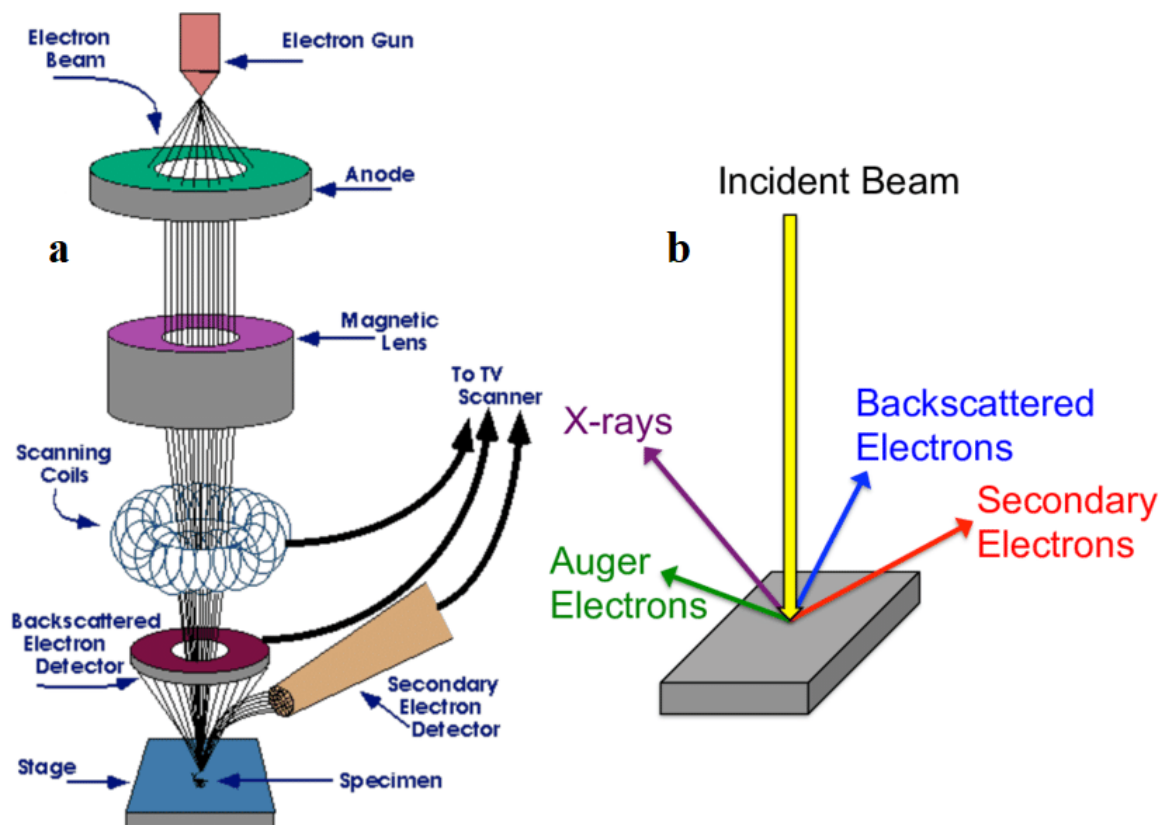


Figure 2.2 Scanning Electron Microscope (SEM) column (a). Sample-beam interactions with SEM (b).²⁹

2.2.2 Ultraviolet-visible spectroscopy (UV/Vis)

a) Absorption of ultraviolet and visible radiation in semiconductors

Absorption of ultraviolet (UV, 200-400 nm) and visible (400-700 nm) radiation of the electromagnetic spectrum is associated with interband electronic transitions, in both atoms and molecules, from lower to higher energy levels. Since the electronic states of the matter are quantized, the amount of photon energy that can be absorbed and cause excitation of electrons from one level to another is specific.

In semiconductors, when the energy of the incident light is about equal to the energy gap of the material, the semiconductor switches from being practically transparent to completely opaque. This light absorption, which leads to the generation of electron-hole pairs, is caused by the excitation of electrons from the valence to the conduction band.

As any process that occurs in nature, the process of light absorption must also obey energy and momentum conservation laws. Since the wavelength of visible light is larger by three orders of magnitude than the lattice parameter, the momentum of light is considered negligible compared to the crystal momentum (k-vector, $|k| = \frac{2\pi}{\alpha}$, where

α is the interatomic distance) in the Brillouin zone. Hence, the absorption of a photon of visible light does not change the momentum of the electron. Interband transitions that preserve the k -vector are called direct transitions. In direct gap semiconductors, the wave vector of the lowest energy state in the conduction band and the highest energy state in the valence band of the material is the same (Figure 2.3a). Hence, electrons can be directly excited by a photon whose energy is greater than the band gap. In contrast, when the position of the conduction band bottom and the valence band top in the k -space is different, the material is characterized by an indirect band gap (Figure 2.3b). In this case, the electron cannot make a direct transition from the top of the valence band to the bottom of the conduction band, as this would violate the conservation of momentum. In order to take place such a transition, the participation of lattice phonons is required. The photon supplies the required energy, while phonon supplies the missing momentum to the electron.³⁰

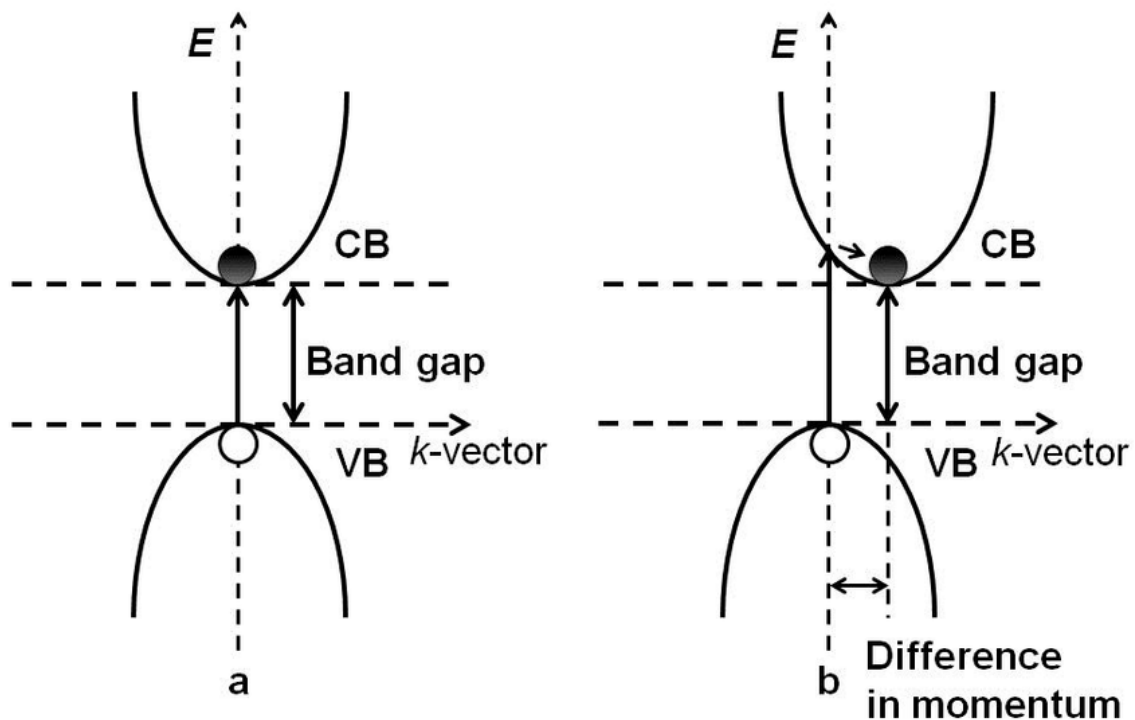


Figure 2.3 Difference between direct and indirect band gap semiconductor.³¹

b) Experimental determination of absorption

UV-Vis spectrophotometer was used to measure the transmittance and reflectance of the samples. The spectrophotometer consists of a light source, which is a deuterium lamp for the UV spectral range and a tungsten lamp for the visible spectral range. The light source is focused on the entrance of a monochromator, which is used to select a single wavelength of all those provided by the lamp source and to scan over the

desired wavelength range. The monochromator is followed by a sample holder and a light detector, used for measuring the intensity of the transmitted or reflected beam from the sample. The set up is connected to a computer which records the data and plots the transmission or reflection spectrum.

Absorbance (A) measures the quantity of light absorbed by a material and can be defined as:

$$A = 1 - T - R \quad (2.1)$$

Reflectance (R) can be defined as the ratio of electromagnetic radiation that is reflected by a surface to the incident radiation, while transmittance (T) is the amount of light transmitted by a surface, normalized by the amount of incident light.

c) Absorption coefficient

When a light beam passes through the matter, it attenuates due to absorption or scattering of photons. This reduction of light intensity can be described by Beer-Lambert law:

$$I = I_0 e^{-\alpha t} \quad (2.2)$$

where I is the light intensity at a distance t into the medium, I_0 is the incident intensity minus the reflection losses at the surface and α is the attenuation coefficient, which in the case of negligible scattering it is named absorption coefficient (Figure 2.4).

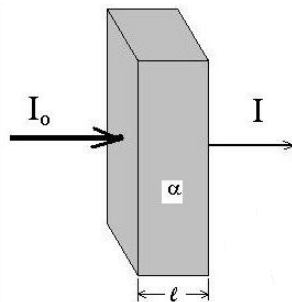


Figure 2.4 The Beer-Lambert law.

The Absorption coefficient for a direct gap semiconductor for allowed interband transitions can be determined by the relation:

$$\alpha = \frac{A(h\nu - E_g)^{1/2}}{h\nu} \quad (2.3)$$

while for indirect allowed transitions by:

$$a = \frac{B(h\nu - E_g)^2}{h\nu} \quad (2.4)$$

d) Energy gap calculation

An estimation of the band gap energy of a semiconductor can be given by using the relation for ideal semiconductors:

$$E_g = \frac{hc}{\lambda_e} \quad (2.5)$$

where h is the Planck's constant, c is the speed of light and λ_e is the wavelength of light absorption. Nevertheless, the crystal structure of a real semiconductor diverges from the ideal one due to the crystallographic defects. Hence, the band gap energy is determined by Tauc's plot method (Figure 2.5). According to this method, the optical band gap for a direct gap semiconductor can be determined from the abscissa of the tangent line of the plotted experimental data of $(\alpha h\nu)^2$ versus incident photon energy ($h\nu$), where absorbance coefficient is zero.

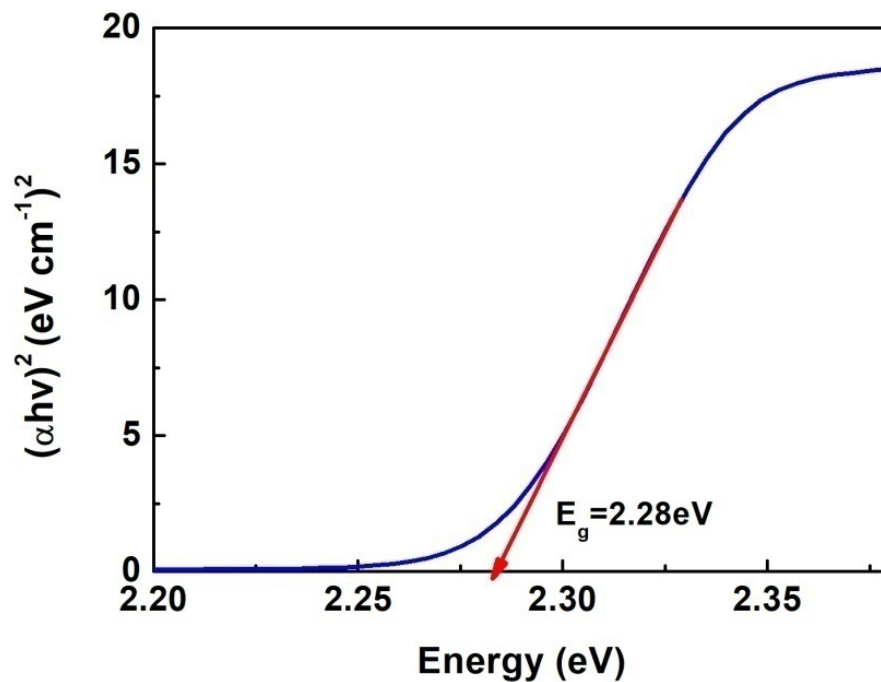


Figure 2.5 Tauc plot for direct gap semiconductor with band energy 2.28eV

2.2.3 X-Ray Diffraction (XRD) ³²

XRD is a characterization technique mainly utilized for chemical phase identification and determination of lattice parameters of a crystalline material based on the recorded diffraction pattern.

X-Rays are generated by a cathode ray tube and filtered to produce monochromatic radiation of K_{α} type. The X-Rays pass through a collimator to adjust the beam width and are directed towards the sample. The samples which are usually crystalline materials are characterized by the orderly periodic arrangement of atoms with typical interatomic distance about 2 to 3 Å, thus, they can be used as three-dimensional diffraction gratings for X-Rays. The scattered X-Rays from the sample interfere with each other either constructively or destructively. XRD is based on constructive interference which is described by Bragg's law:

$$n\lambda = 2d \sin\theta \quad (2.6)$$

Bragg's law relates the wavelength (λ) of the incident wave to the diffraction angle (θ) and the lattice spacing (d) in a crystalline material (Figure 2.6). The diffracted X-Rays that satisfy the Bragg's law are detected and the angles are recorded.

The diffraction pattern generated by XRD analysis is a reciprocal space representation of the crystal lattice. In particular, the position of the diffraction peaks are a function of unit cell parameters while the diffracted intensities are a function of chemical elements and their spatial arrangement in the unit cell. Hence, the diffraction pattern is considered to be a unique 'fingerprint' of the crystal structure of the sample and can be used for the identification of a single or multiple phases in the sample.³³

In order to determine the unit cell lattice parameters from the peak position, it is necessary to assign to each peak the appropriate Miller indices (hkl) and identify the existing Bravais lattice. Hence, considering the d-spacing equation for the sample's crystal structure and combining it with Bragg's law, the lattice parameters can be calculated.

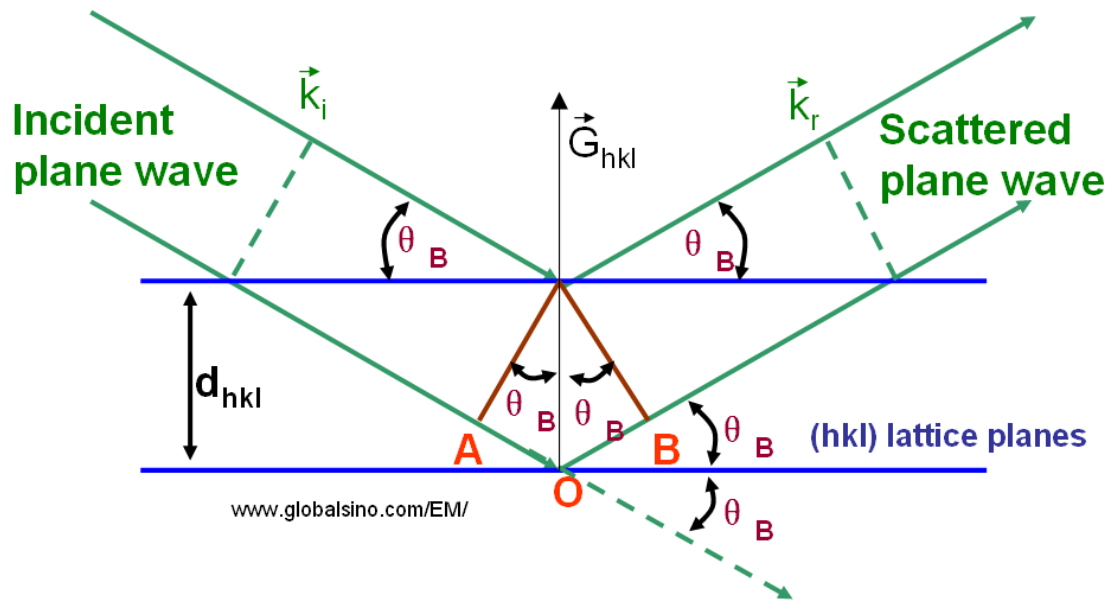


Figure 2.6 Schematic representation of Bragg condition and Bragg's law.³⁴

2.3 Gas sensing experimental set up

Gas sensing measurements were performed in a home-made gas sensing chamber (Figure 2.7), which allows the electrical characterization of the sensors in a controlled atmosphere. The gas sensing assembly consists of a certified gas supplier, in this case synthetic air, connected with mass flow controllers and a stainless chamber which was initially evacuated down to 10^{-3} mbar. A commercial ozone analyzer (Thermo Electron Corporation, Model 49i) was used to supply and record well defined ozone concentrations which are inserted in the chamber with a 500 sccm (standard cm^3/min) flow. Electrical measurements were carried out by an electrometer (Keithley 6517A) at room temperature by applying a constant voltage of 1V. During the experimental process the pressure in the chamber was kept constant and equal to 400 mbar.

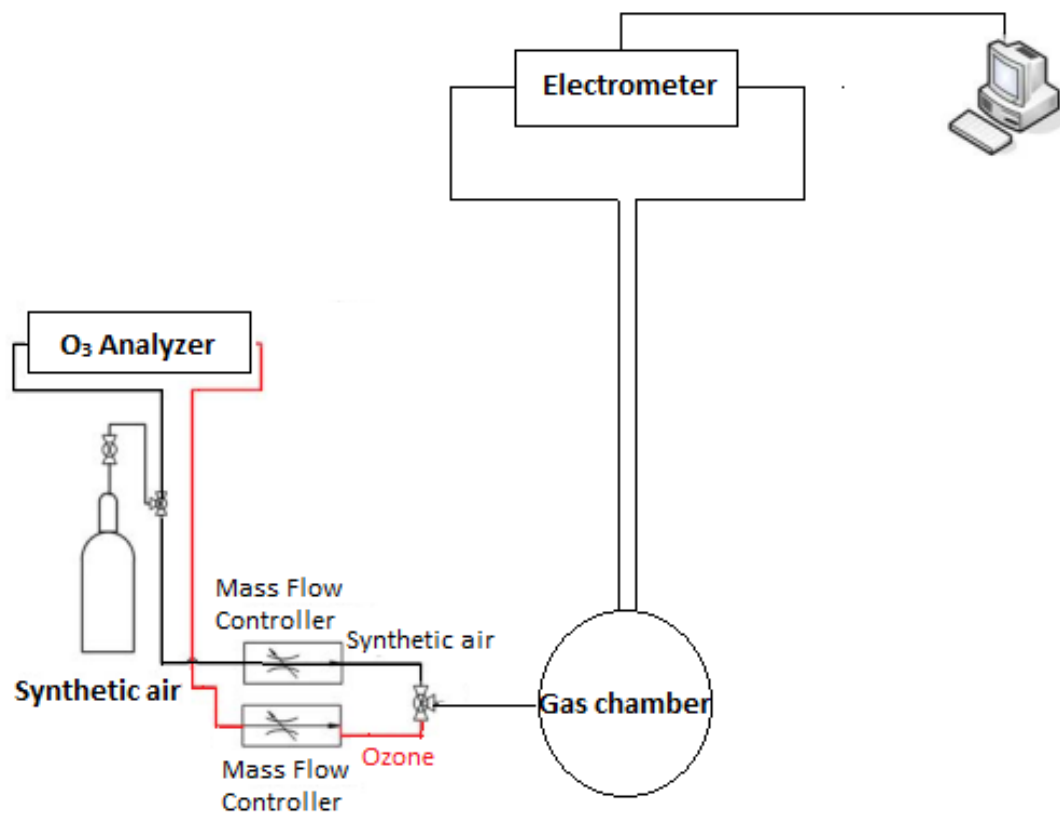
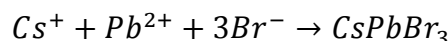


Figure 2.7 Schematic diagram of gas sensing assembly

CHAPTER 3: MORPHOLOGY, STRUCTURE AND OPTICAL PROPERTIES

3.1 Reaction procedure and nanocrystal formation

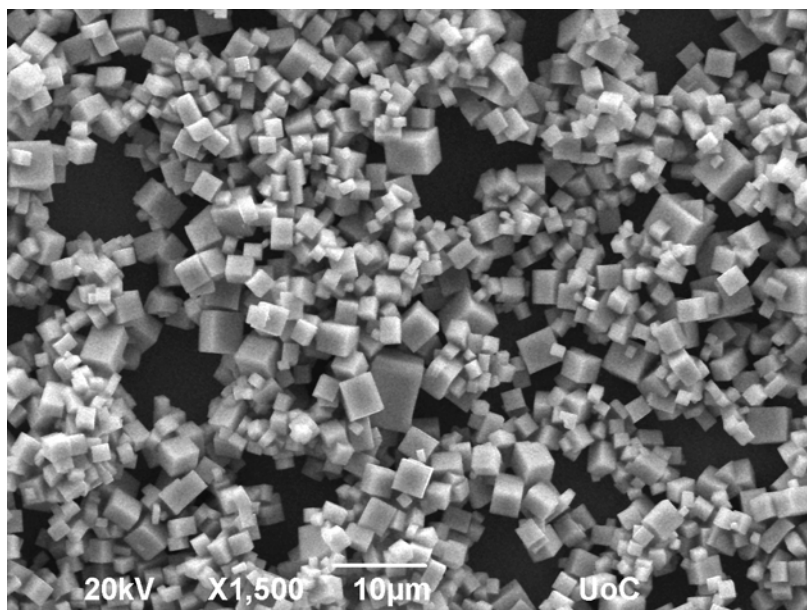
The perovskite nanocrystals were fabricated via a facile room temperature precipitation method as described in the section 2.1. A mixture of PbBr₂ and CsBr precursors was dissolved in Dimethylformamide (DMF). The high polarity of the solvent (DMF) allows polar reactants (ion sources) to be dissolved. The concentration of CsBr and PbBr₂ is much smaller than their solubility in DMF, indicating that they can be well dissolved without any crystallization effect. Crystallization occurs when the solubility of a solute in a solution is reduced by some means, such as the addition of an antisolvent. This implies that the solution will become supersaturated. In order for supersaturation and precipitation to take place, toluene was added to the above solution. As solubility is reduced to a point where crystals will nucleate and then grow according to reaction:



All-inorganic lead halide perovskite nanocubes with sizes ranging from 500 to 1000nm have been fabricated directly on the substrate in both Ar atmosphere (Figure 3.1a) and ambient conditions (Figure 3.1b). In the first case, well-crystalline ligand-free CsPbBr₃ nanocubes with sharp edges were formed and remained stable after their exposure at ambient conditions. In contrast, distorted ligand-free CsPbBr₃ nanocubes with deformed edges and slightly smaller size were fabricated under ambient conditions.

The difference in the morphology can be attributed to the different crystallization environment during the synthesis. It is known that the exposure of lead halide perovskites in traces of water during the re-precipitation synthesis method can affect the final morphology of the NCs.³⁵

a



b

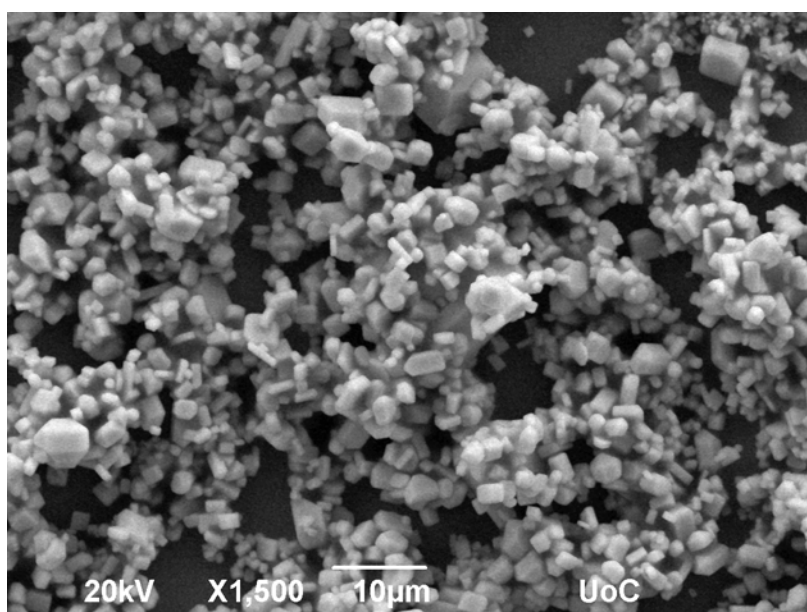


Figure 3.1 SEM images of well-formed (a) and distorted (b) CsPbBr₃ nanocubes.

3.2 Structure determination of the perovskite nanocubes

The crystal structure of the synthesized samples was investigated by X-Ray Diffraction. The XRD patterns exhibit sharp diffraction peaks, revealing the high crystallinity of the samples (Figure 3.2a). Moreover, the patterns of both samples match well with orthorhombic phase of CsPbBr₃ (Figure 3.2b). In particular, the

patterns exhibit similar Bragg's peaks at $2\theta = 15.2^\circ, 21.4^\circ, 30.6^\circ, 37.7^\circ$ and 43.7° corresponding to (110), (112), (220), (132) and (224) planes of the orthorhombic phase respectively. However, the distorted CsPbBr_3 sample exhibits some additional low-intensity peaks at $2\theta = 11.6^\circ$ and 24.1° , indicating the existence of the secondary tetragonal phase CsPb_2Br_5 with crystallographic planes (002) and (210) respectively (Figure 3.3). The formation of this secondary phase with reduced dimensionality is associated with a water-induced transformation from CsPbBr_3 orthorhombic phase due to synthesis environment.³⁶

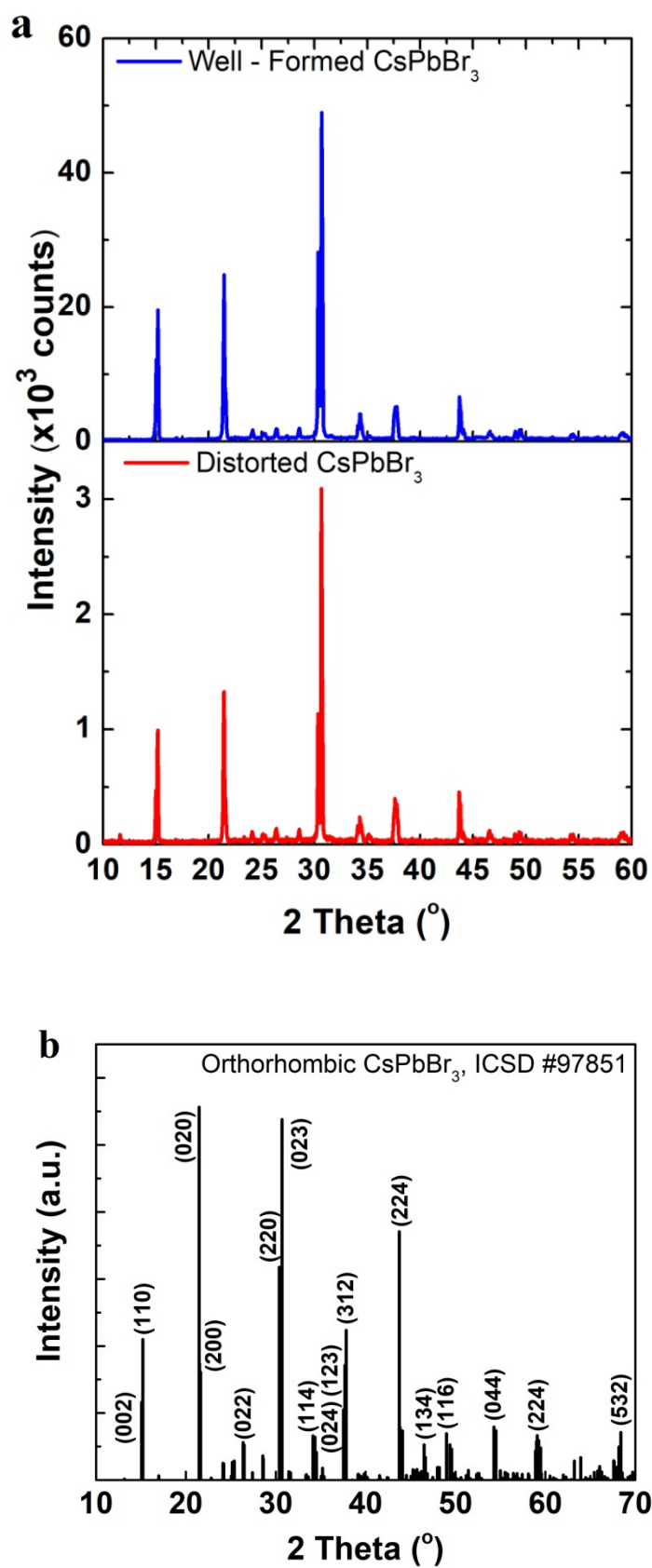


Figure 3.2 XRD patterns of well-defined (blue curve) and distorted (red curve) CsPbBr₃ NCs (a). Reference pattern of the orthorhombic CsPbBr₃ crystal structure (black curve)

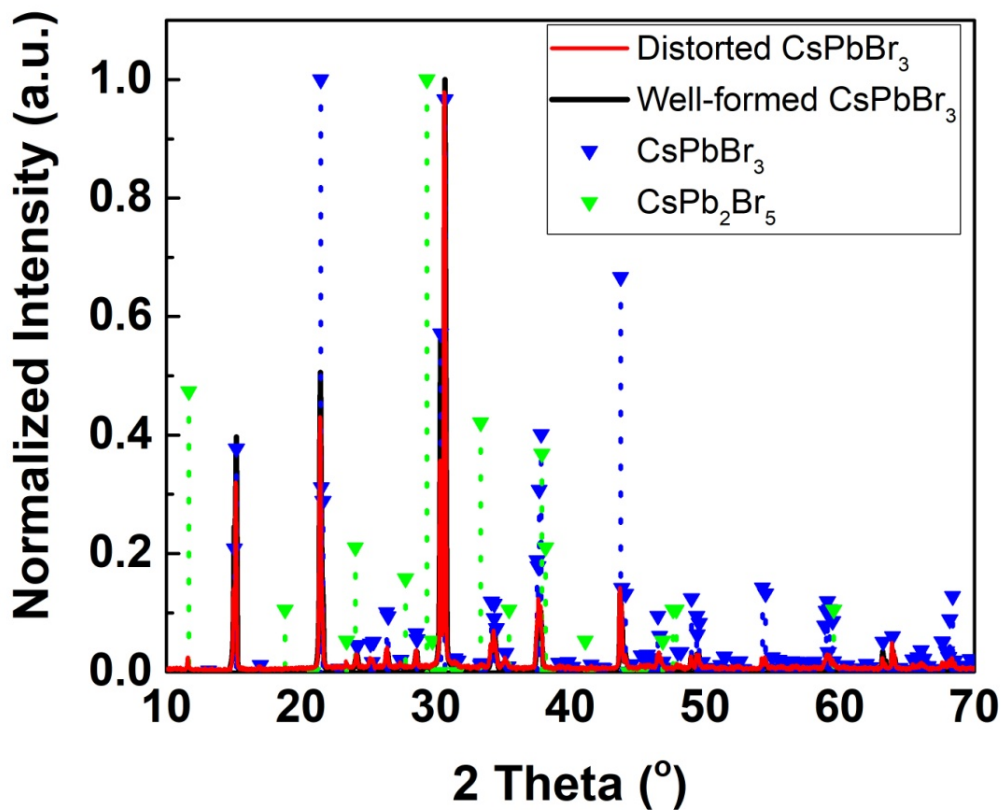


Figure 3.3 Comparison of experimental XRD patterns (black and red curves) with reference patterns of orthorhombic CsPbBr_3 (blue line) and tetragonal CsPb_2Br_5 (green line) crystal structures.

Moreover, elemental analysis was performed by EDS, confirming the atomic ratio of Cs:Pb:Br is 1.2:1:3.4 for the sample synthesized at Ar atmosphere (Figure 3.4a). While the same analysis for the sample fabricated at air (distorted cubes) revealed an atomic ratio of Cs:Pb:Br is 1.2:1:3.5 (Figure 3.4b).

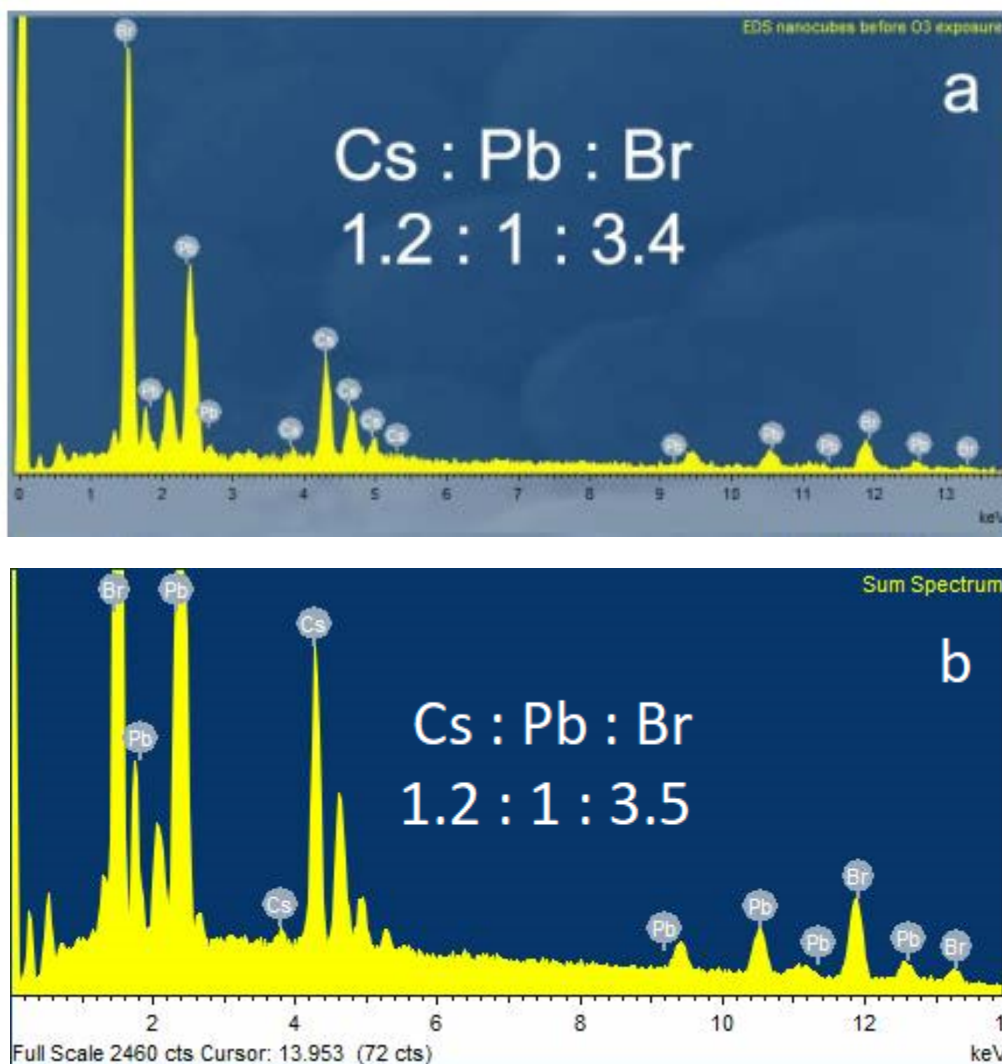


Figure 3.4 SEM-EDS spectra of well-formed (a) and distorted (b) CsPbBr₃ nanocubes.

3.3 Optical properties of the CsPbBr₃ nanocubes

UV-Visible absorption was studied for the as synthesized samples. Figure 3.5 presents the absorption spectra of well-defined and distorted all-inorganic perovskites. Both samples show a sharp absorption band-edge at 544 nm and behave as direct gap semiconductors. Moreover, the band energy for both samples was estimated by Tauc plot method at 2.28 eV (Figure 2.5).

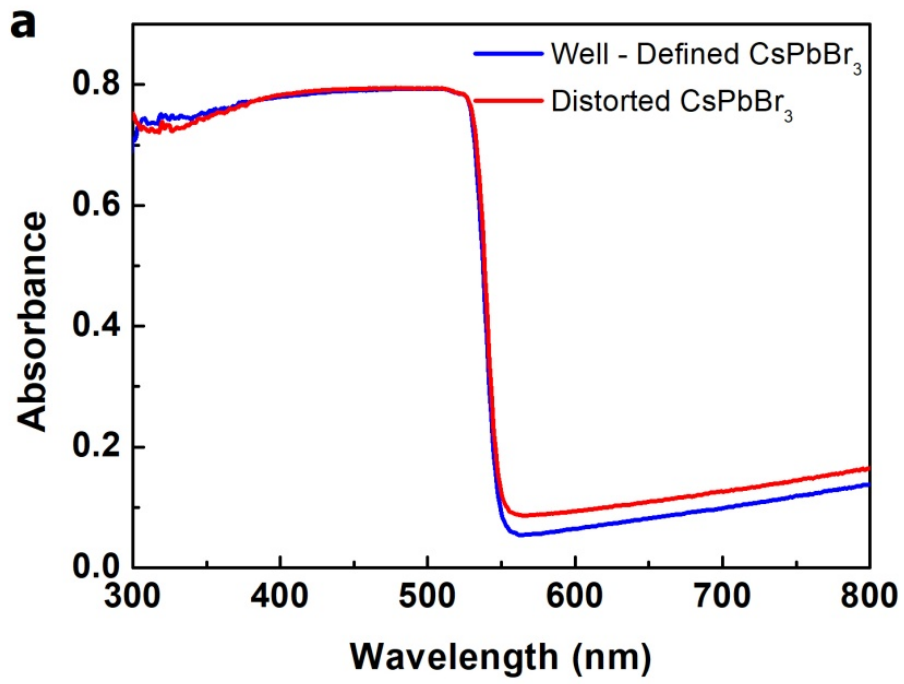


Figure 3.5 Absorption spectra of well-defined (blue curve) and distorted (red curve) all-inorganic perovskites.

CHAPTER 4: ALL-INORGANIC LEAD HALIDE NANOCUBES AS GAS SENSORS

4.1 Perovskite nanocubes sensors

The great demand to detect and monitor a broad range of volatile and other harmful gases has led to a significant development of gas sensing technologies. In particular, gas sensors have a wide variety of applications, including environmental monitoring, public safety and air conditioning systems.^{37, 38, 39}

Among the gas sensors, the sensors that detect ozone and hydrogen hold a prominent role due to the harmful effects of both gases. Ozone (O_3) is naturally produced, in small concentrations, in the stratosphere where UV light from the sun splits an oxygen molecule (O_2), forming two single oxygen atoms. When a freed atom collides with an oxygen molecule, ozone is generated. Stratospheric ozone it is also called 'good' ozone, since it protects the Earth's surface from UV light. Ozone can also be detected in the troposphere. Tropospheric ozone, also known as 'bad' ozone, is produced from the reaction between nitrogen oxides and hydrocarbons emitted by cars and industrial releases.

It is well known that high concentrations of ozone gas in the ambient atmosphere are hazardous to human health. When its concentration to air exceeds 1 ppm, a variety of health problems such as chest pain, coughing, throat irritation and even more severe such as bronchitis and asthma can be caused.⁴⁰ Ozone concentrations higher than 50 ppm present risks to life and concentrations higher than 1000 ppm can cause death in short time.⁴¹ Therefore, the need for ozone sensors is crucial. In order to improve the detection of ozone, it is necessary to develop both effective and inexpensive devices for the continuous monitoring of its concentrations.

The ozone sensors can be classified based on the sensing principle as optical⁴², optochemical⁴³, electrochemical⁴⁴ and conductometric⁴⁵. The operational fundamental principle of a conductometric sensor is the change in resistance due to reactions that occur on the surface of the sensing layer. In this case, the sensing materials are metal oxides such as, In_2O_3 , SnO_2 , WO_3 , ZnO , MoO_3-TiO_2 , Fe_2O_3 and $SmFeO_3$.⁴⁶ However, most of these systems need to operate at temperatures well above room temperature in order to demonstrate sensitivities down to few hundreds of ppb and they are not suitable for self-powered devices since they require to be switched on before their operation by external stimuli.

On the contrary, hydrogen is the most abundant chemical element in the universe. At room temperature and atmospheric pressure, pure hydrogen exists as a diatomic gas (H_2) in concentrations less than 1 ppm.⁴⁷ Hydrogen gas is extensively used in many industrial fields such as the synthesis of ammonia and methanol, the hydration of hydrocarbons, the production of rocket fuels and metal refining and is the most attractive candidate for future fuel and energy carrier. However, due to its small

molecular volume, hydrogen gas is prone to leakage. Hydrogen gas is colorless, odorless, tasteless and highly explosive when its concentration to the air exceeds the 40000 ppm.^{48, 49} Therefore, the need for its detection and concentration monitoring is essential.

Hydrogen sensors can be classified according to the detection technology as catalytic, thermal conductivity, electrochemical, resistance based, work function based, mechanical, optical and acoustic. Resistance based sensors include a variety of semiconducting oxides such as SnO₂,⁵⁰ ZnO,⁵¹ TiO₂,⁵² FeO, Fe₂O₃, NiO, In₂O₃⁵³ and WO₃.⁵⁴ When exposed to hydrogen, these sensors show a great change in their electrical resistance. Although, their operating temperature is well above room temperature, which could raise the possibility of triggering an explosion, and their sensitivity is limited to few hundreds of ppm. Hence, it is necessary to develop cost effective ultrasensitive hydrogen gas sensors, working at room temperature without any power sources.

The present work is the first to demonstrate the application of all-inorganic lead halide nanocrystals as ozone and hydrogen sensing materials with superior operation stability. Furthermore, the variations of the sensing ability of the nanocubes synthesized in Ar and in air will be evaluated.

4.2 CsPbBr₃ Nanocubes for ozone gas sensing

a) Sensing properties of well-defined CsPbBr₃ nanocubes

The ozone sensing properties of well-formed CsPbBr₃ nanocubes were investigated by electrical measurements at room temperature. The sample was placed into the homemade chamber (Figure 2.7) and the sensing process was carried out at a pressure of 400mbar. The initial current was measured to be approximately 2μA (Figure 4.1) without external stimulus. This high initial current value is due to the exposure of the sample in ambient light. CsPbBr₃ nanocubes show a sharp absorption edge at 544nm with band gap energy 2.28eV (Figure 3.5), which implies that the sensor absorbs in the visible region of the electromagnetic spectrum.

The sensing process was initiated by exposing the sample to well-controlled ozone concentrations ranging from 2650ppb to 4ppb. As demonstrated in Figure 4.1 the electrical current increases instantly after the sample's exposure to ozone gas till a maximum current value. Then, the sample's recovery till a minimum current value was followed by introducing synthetic air in the chamber. The same behavior was observed for all the tested concentrations.

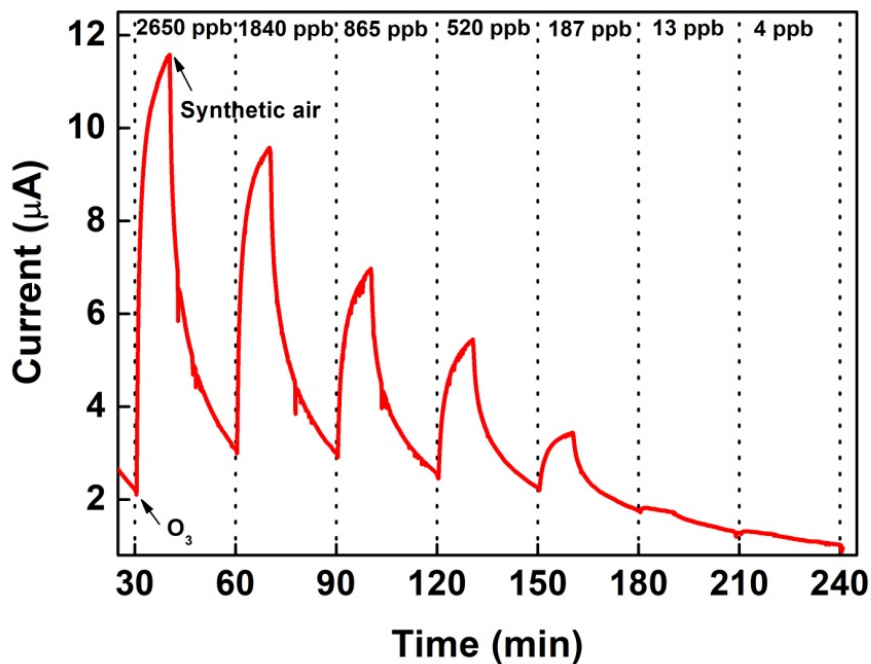


Figure 4.1 Electrical response of well-formed CsPbBr₃ as sensing material upon various ozone concentrations as a function of time.

For a further investigation of the ability of the sensor to resolve low ozone concentrations, the normalized exponential decay curves during the oxidation processes at the corresponding ozone concentrations as a function of time were plotted (Figure 4.2). Although the responses of higher ozone concentrations are well separated from each other, in concentrations lower than 13 ppb the exponential curves cannot be distinguished, implying the disability of the sensor to resolve ultra low ozone concentrations.

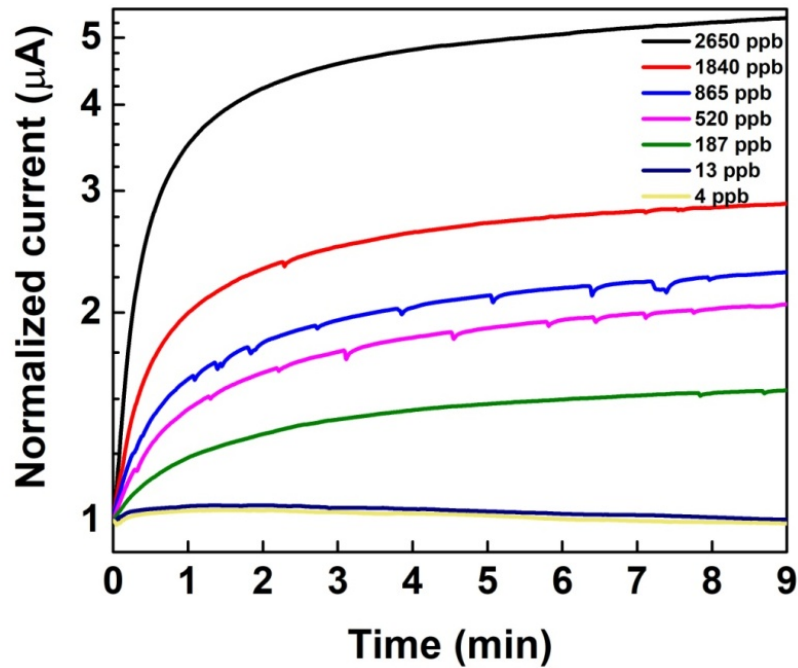


Figure 4.2 Normalized exponential decay curves upon ozone concentration as a function of time.

The performance of a gas sensor is also characterized by its sensitivity (S), which can be defined as:

$$S\% = \frac{I_{max} - I_{min}}{I_{min}} \times 100 \quad (4.1)$$

Where I_{max} and I_{min} are the maximum and minimum current values in the presence and absence of ozone gas respectively. Figure 4.3 represents the evolution of I_{max} and I_{min} as a function ozone concentration. It is noted that as ozone concentration increases, maximum current values increase as well, while minimum current values remain almost constant. As a consequence, the sensitivity of the nanocubes is affected by the ozone concentration. In particular, sensitivity is increasing from 1.3% for 4 ppb to 428% for 2620 ppb, with 187 ppb being the point that the sensor can measure in certainty with 54% sensitivity.

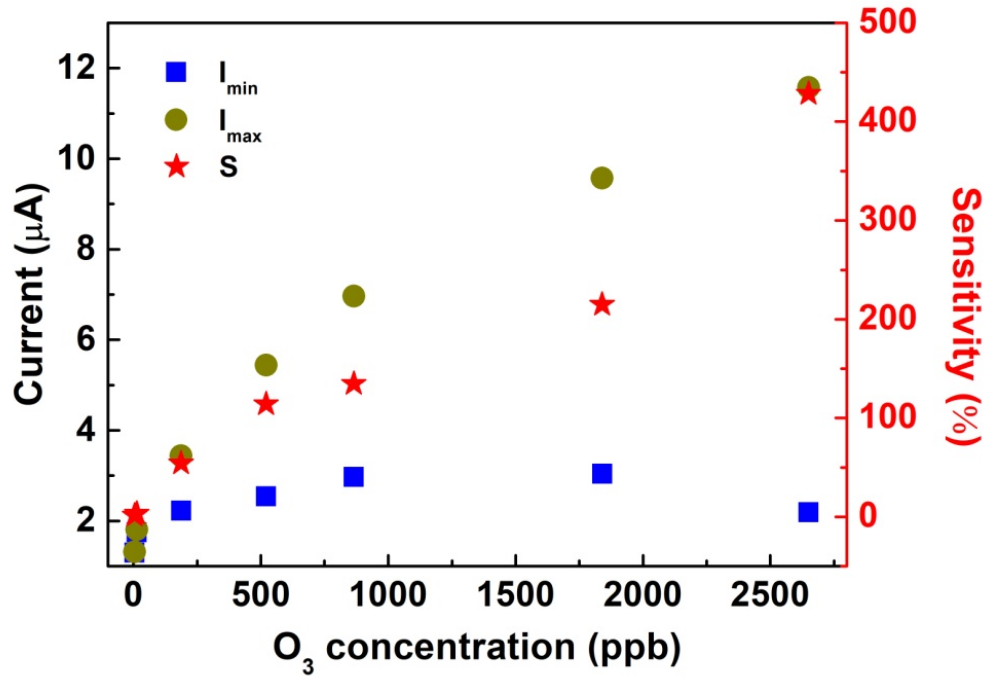


Figure 4.3 Sensitivity as a function of ozone concentration

Response and recovery times are also two important parameters that characterize the performance of a gas sensor. Response (t_{res}) and recovery (t_{rec}) times are calculated by the equations:

$$I = \begin{cases} I_0 + A_d + A_g \left(e^{-\frac{t_c}{t_{res}}} - e^{-\frac{t}{t_{res}}} \right), & I \leq I_0 \\ I_0 + A_d e^{-\frac{t-t_c}{t_{rec}}}, & I > I_0 \end{cases} \quad (4.2)$$

Where I_0 is the initial current value, A_d and A_g are the decay and growth amplitudes respectively and t_c is the time where current reaches its maximum value. Figure 4.4 shows the evolution of t_{res} and t_{rec} with the ozone concentration and it can be noticed that the response times lie between 100 and 150 s, while the recovery times lie between 250 and 320s. Moreover, the response time is almost stable for concentration lower than 865 ppb and decreases for higher concentrations. In contrast, recovery time decreases as the ozone concentration increases.

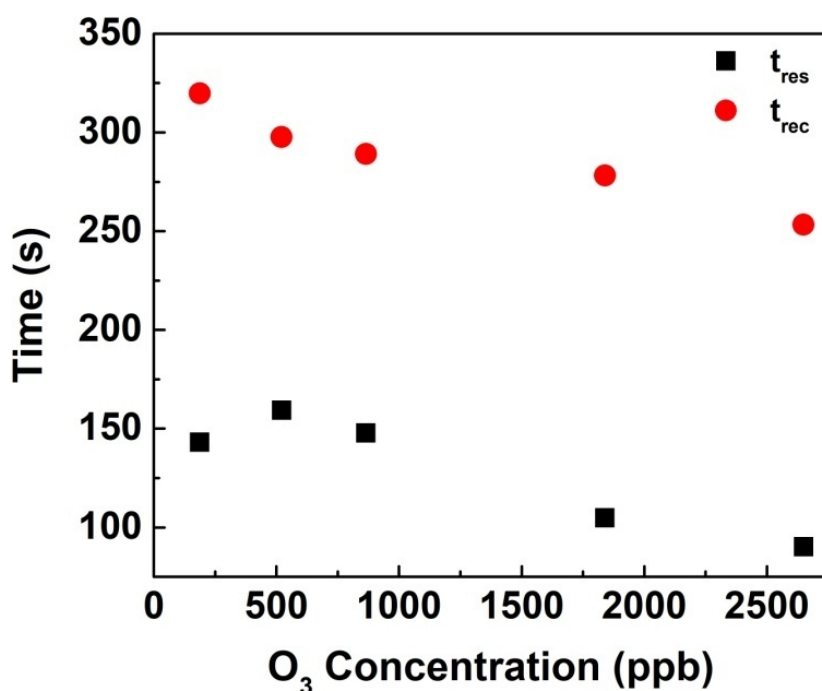


Figure 4.4 Response and recovery times as a function of O₃ concentration of well-formed CsPbBr₃ nanocubes.

b) Stability of well-defined nanocubes as ozone sensing material

Two important features for the application of a material for sensing are the short-term and long-term stability of the fabricated sensor. Short-term stability is connected with the repeatability of sensor characteristics during certain time at working conditions. In order to examine the short-term stability of the sensor, a number of ozone/synthetic air switching cycles took place (Figure 4.5). Each cycle was characterized by a current increase as the ozone flew in the chamber and a current decrease to its initial value when the ozone gas was replaced with synthetic air. This behavior was observed for four ozone/synthetic air cycles and can be attributed to the high crystallinity of the nanocubes. However, it was noticed that after a number of successive air switching cycles the current did not fully reverse to its initial state, possibly due to residual adsorbed ozone molecules. By the end of this process, SEM imaging and EDS analysis confirmed that the nanocubes retain their morphology and stoichiometry (Figure 4.7a, b).

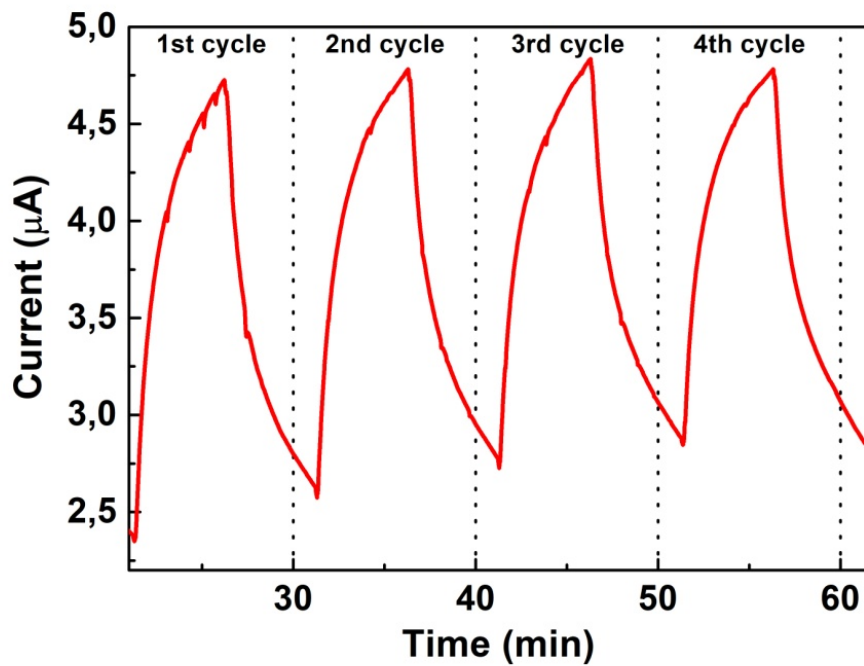


Figure 4.5 Time dependence of ozone response upon four successive cycles.

Long-term stability is connected with retaining the electrical behavior after a period of time at normal storage conditions. In order to check the long-term stability, the sensor was stored under ambient conditions for three months. In this case, it was noticed that the current values were higher, although, the trend of the electrical response is same as the first air switching cycle for all ozone concentrations ranging from 2650 ppb to 4 ppb (Figure 4.6).

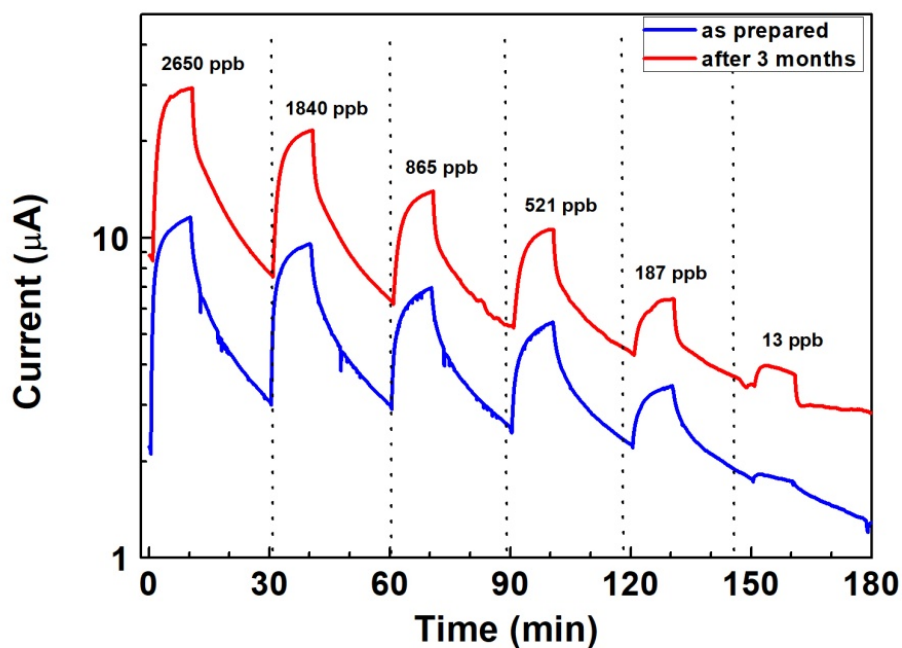


Figure 4.6 Comparison of electrical responses of well-defined CsPbBr₃ sensor as a function of time, in the as prepared state (blue curve) and the same sample after three month storage at ambient conditions (red curve).

In order to evaluate the reason of the long-term stability the XRD patterns of the stored sample was compared to the as-prepared one (Figure 4.8). This comparison revealed that, even when the sample was exposed to ambient conditions, no phase alteration occurred. SEM imaging and EDS analysis also confirm that the nanocubes retain their shape and stoichiometry (Figure 4.7).

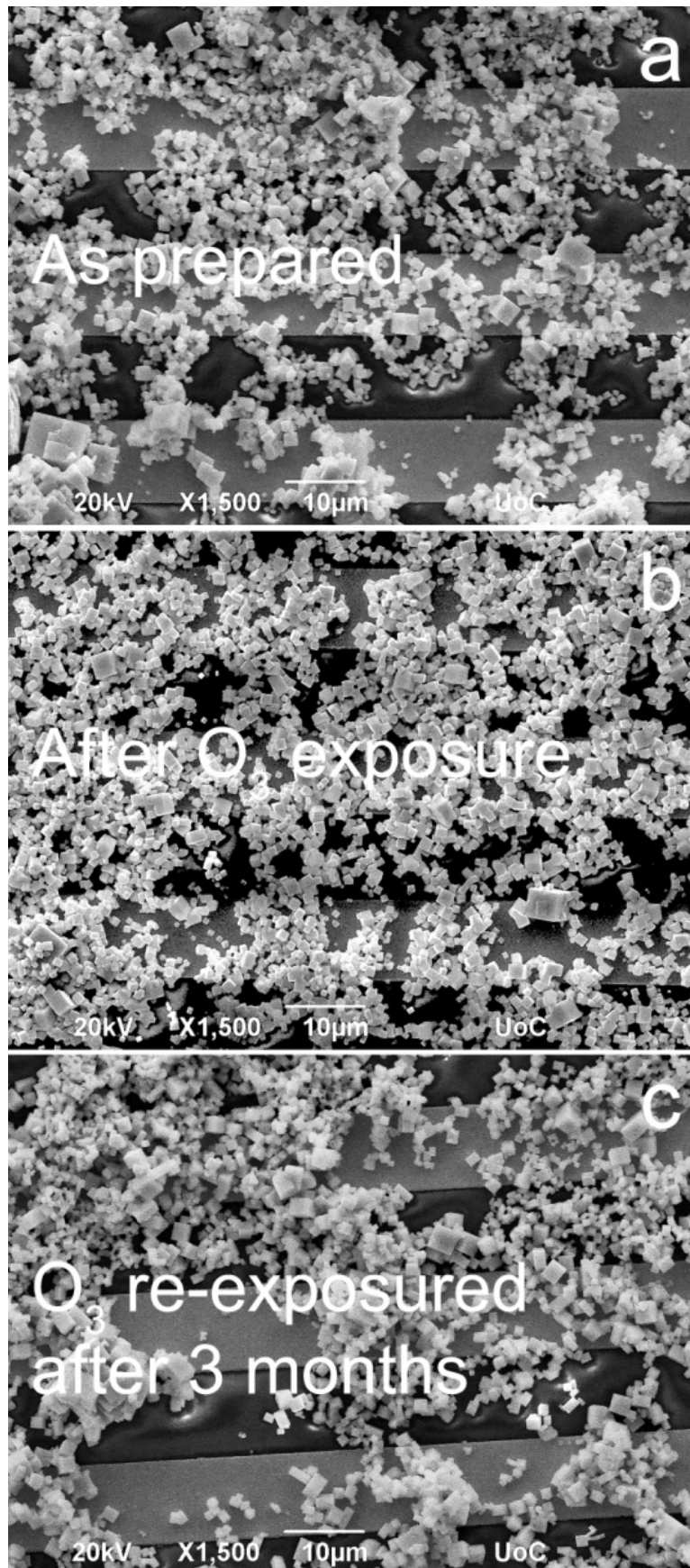


Figure 4.7 SEM images before ozone exposure (a), after ozone exposure (b) and ozone re-exposure after three months of storage under ambient conditions (c).

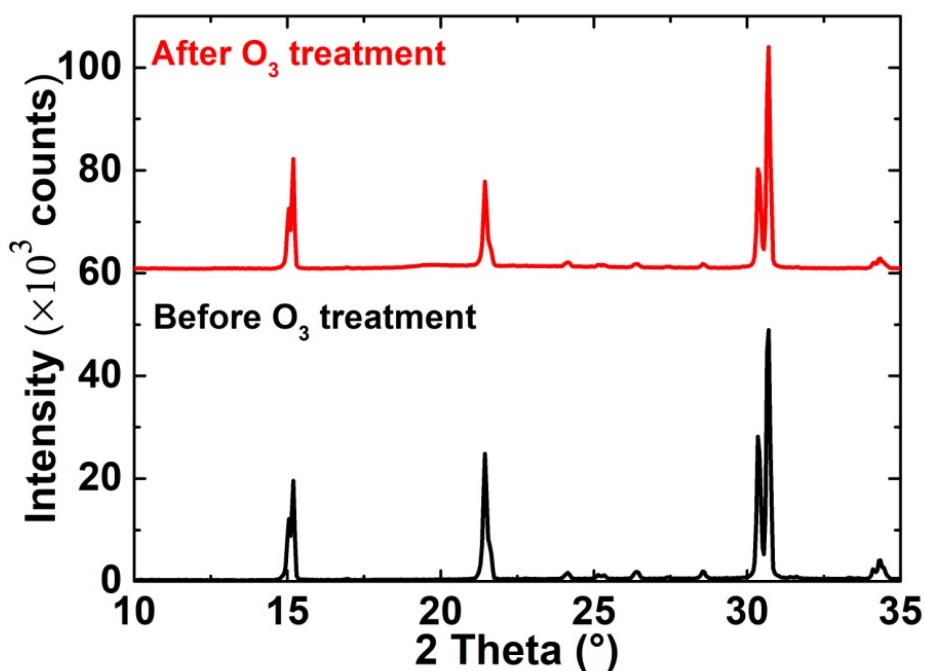


Figure 2.8 XRD patterns of well-formed CsPbBr₃ nanocubes before (black curve) and after (red curve) O₃ treatment.

c) Sensing properties of distorted CsPbBr₃ nanocubes

The high performance of well-formed nanocubes as ozone sensing material was a motivation for the fabrication of an even simpler and cost-effective ozone sensor. Consequently, the ozone sensing properties of distorted CsPbBr₃ nanocubes were also investigated. The sensor was placed in the gas-sensing chamber, which was evacuated down to 10⁻³ mbar. At that time, it was noticed that by applying a voltage of 1V, the initial current value was approximately 3μA. This high initial current value can be attributed to the sharp absorption edge at 544 nm with band gap energy 2.28eV (Figure 3.5), indicating that the distorted nanocubes absorb in the visible range.

Subsequently, the sample was exposed to ozone gas of well-defined concentration with a flow of 500 sccm (standard cubic centimeters per minute) for ten minutes, leading to an increase of electrical current. Then, the ozone gas was replaced by synthetic air and the sensor was recovered for twenty minutes. The sample was exposed to different ozone concentrations ranging from 2620 ppb to 4 ppb (Figure 4.9). The pressure in the chamber during the measurements remained constant at 600 mbar.

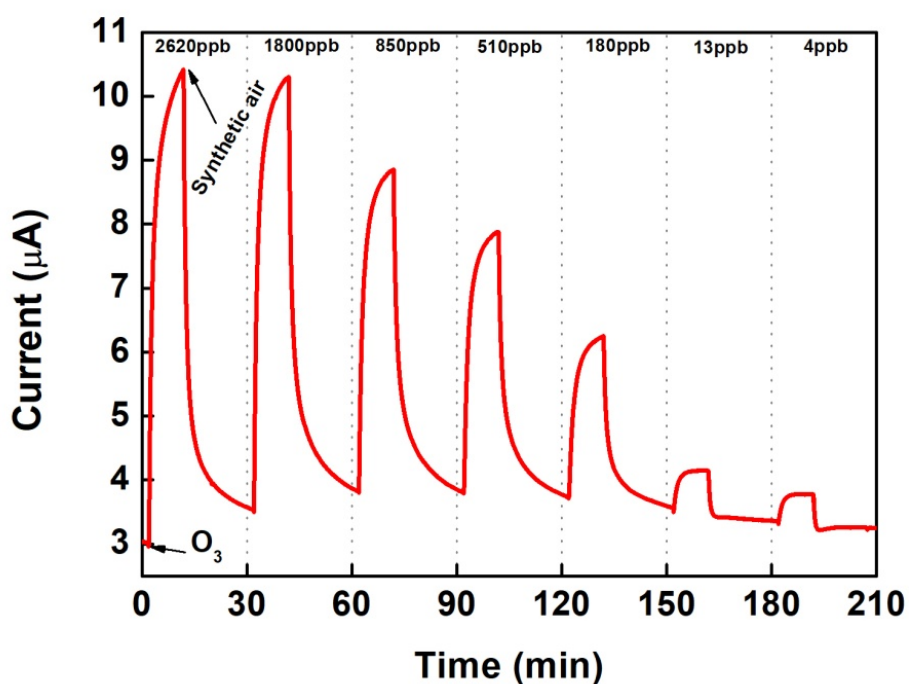


Figure 3.9 Electrical response of distorted all-inorganic perovskite nanocubes as a function of time upon various ozone concentration ranging from 2620 ppb to 4 ppb.

In addition, the normalized comparison of the exponential decay curves at all tested ozone concentrations was made in order to examine the ability of the sensor to ‘understand’ different concentrations (Figure 4.10). As shown in Figure 4.10 the sensor is able to detect and separate ultra-low concentrations at the level of 4ppb with 13% sensitivity (Figure 4.11). It is also worth mentioning that the maximum current value decreases upon decreasing O_3 concentration, which is not the case for the minimum current value, which is almost constant, especially in lower O_3 concentrations. Hence, the sensitivity of the sample, which was derived from equation 4.1, is decreasing from 250% for 2620ppb to approximately 13% for 4ppb, as expected. Furthermore, response times lie between 74s and 123s, while recovery times lie between 33s and approximately 132s (Figure 4.12). Notably, response time is almost stable for concentrations between 510ppb and 2620ppb. On contrast, recovery time increases as O_3 concentration increases from 4ppb to 510ppb, while decreases as concentration increases from 510ppb to 2620ppb.

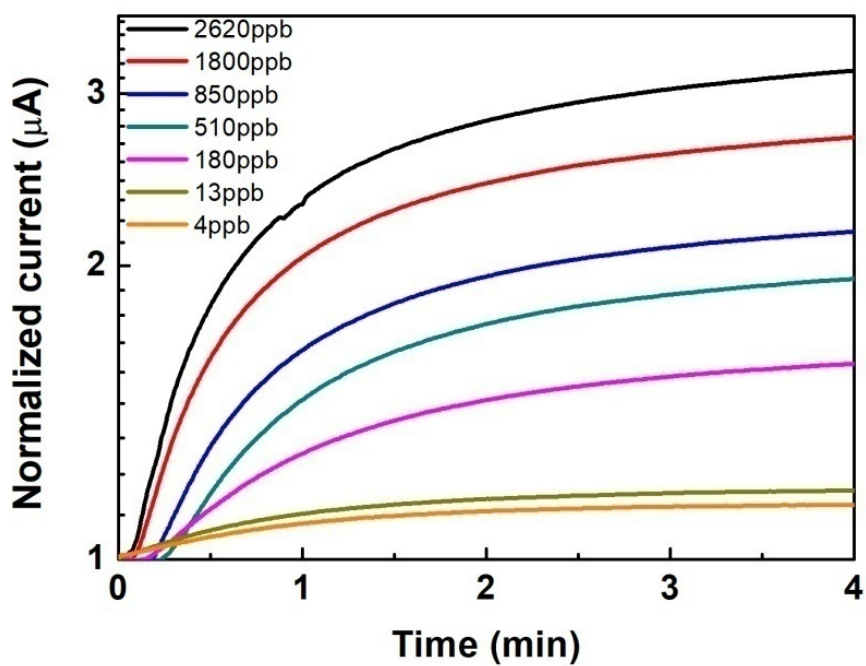


Figure 4.10 Normalized exponential decay curves of distorted CsPbBr₃ upon ozone concentration as a function of time.

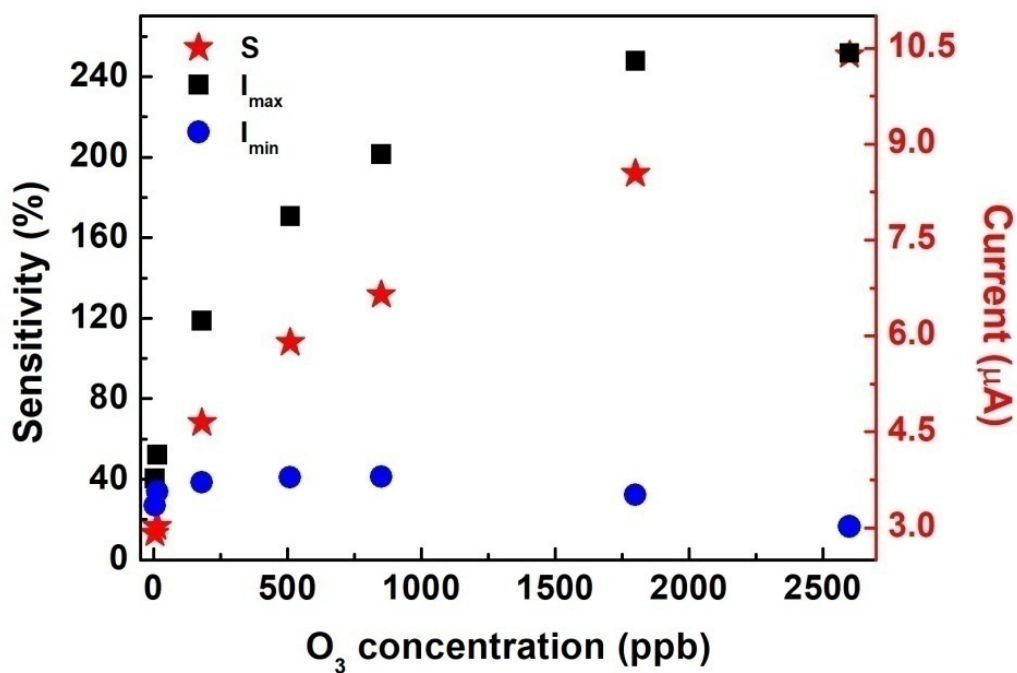


Figure 4.11 Sensitivity of distorted CsPbBr₃ nanocubes as a function of ozone concentration.

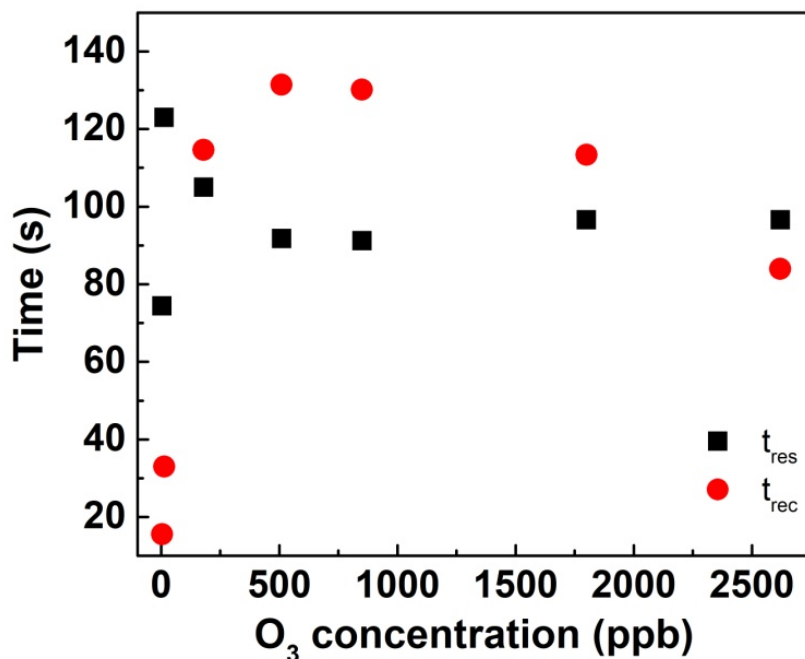


Figure 4.12 Response and recovery times as function of O₃ concentration of distorted CsPbBr₃ nanocubes.

d) Stability of distorted CsPbBr₃ nanocubes as ozone sensing materials.

In order to test the repeatability of the sensor, four ozone/synthetic air switching cycles took place (Figure 4.13). At this point, ozone concentration remained constant at 510ppb. Following ozone exposure, the induced current was increased, while its removal led to current decrease to its initial value (Figure 4.13). Moreover, SEM imaging and EDS analysis revealed that after those successive O₃/synthetic air switching cycles, the sample retains its morphological and stoichiometric features (Figure 4.14).

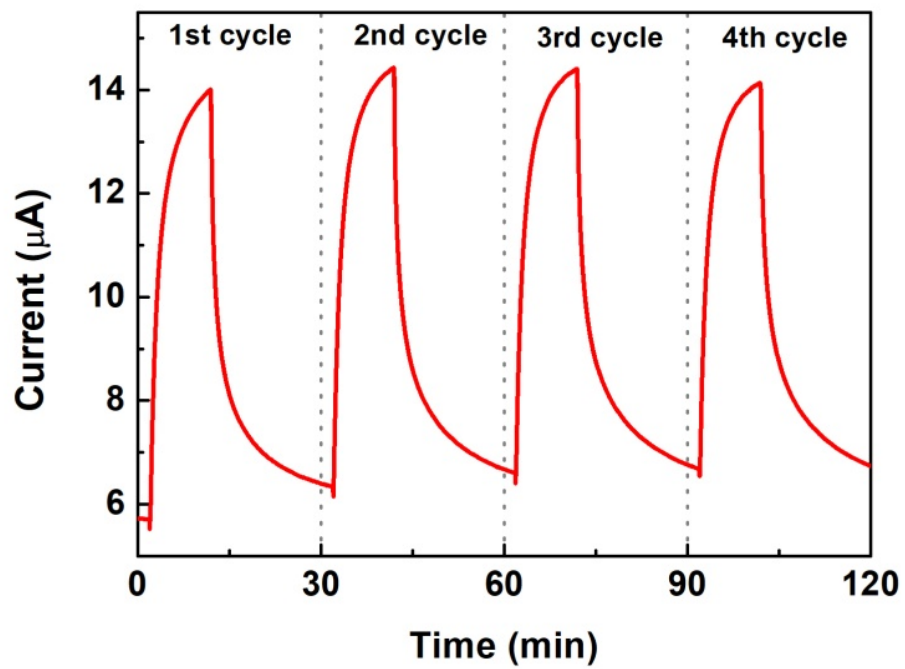


Figure 4.13 Electrical response of distorted all-inorganic nanocubes as sensing material after four successive cycles as a function of time.

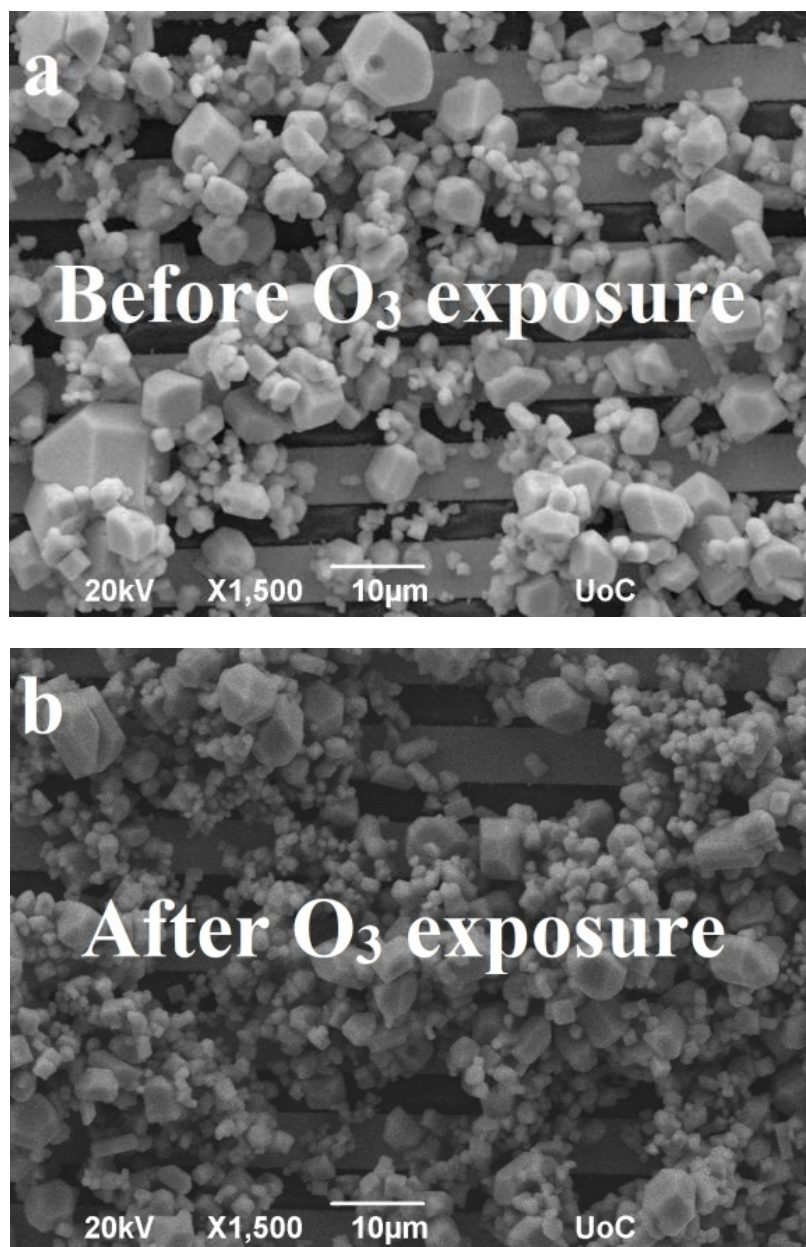


Figure 4.14 SEM images of distorted CsPbBr₃ before (a) and after (b) O₃ exposure.

e) Comparison of ozone sensors

Gas sensors have been a subject of intensive research and development efforts. There is a high demand in sensors that can quickly and reliably detect ozone over a wide range of oxygen and moisture concentrations. Consequently, the comparison of well-formed and distorted all-inorganic lead halide nanocubes as ozone sensors is necessary.

In terms of cost, both sensing elements are worthwhile as they are produced through facile and simple chemical methods. However, distorted nanocubes are more

inexpensive and less time consuming since they are synthesized under ambient conditions.

In addition, the gas sensing properties of the under-studying ozone sensors are also compared. Figure 4.15 demonstrates the electrical response of both well-formed and distorted sensing materials upon various ozone concentrations ranging from approximately 2650ppb to 4ppb as a function of time. It can be observed that in both cases the current intensity increases in the presence of ozone gas, while it decreases upon ozone removal. Therefore, distorted nanocubes display significantly higher electrical response as the ozone concentration decreases down to 4ppb where the performance of well-formed nanocubes is almost absent. As a consequence, the sensitivity of distorted sensing element at lower ozone concentrations is by far better than well-shaped CsPbBr_3 sensor, with values ranging from approximately 250% to 13% for 2650ppb and 4ppb of ozone respectively (Figure 4.16 a, b). On the other hand, the sensitivity of well-formed perovskite sensor is almost 430% at 2650ppb, while it drops dramatically to 1.50% at 4ppb. Accordingly, at 187ppb, which corresponds to the concentration that well-formed CsPbBr_3 nanocube sensor can measure with certainty, its sensitivity is approximately 54%, while at the same ozone concentration distorted CsPbBr_3 sensor displays sensitivity of 68% (Figure 4.19).

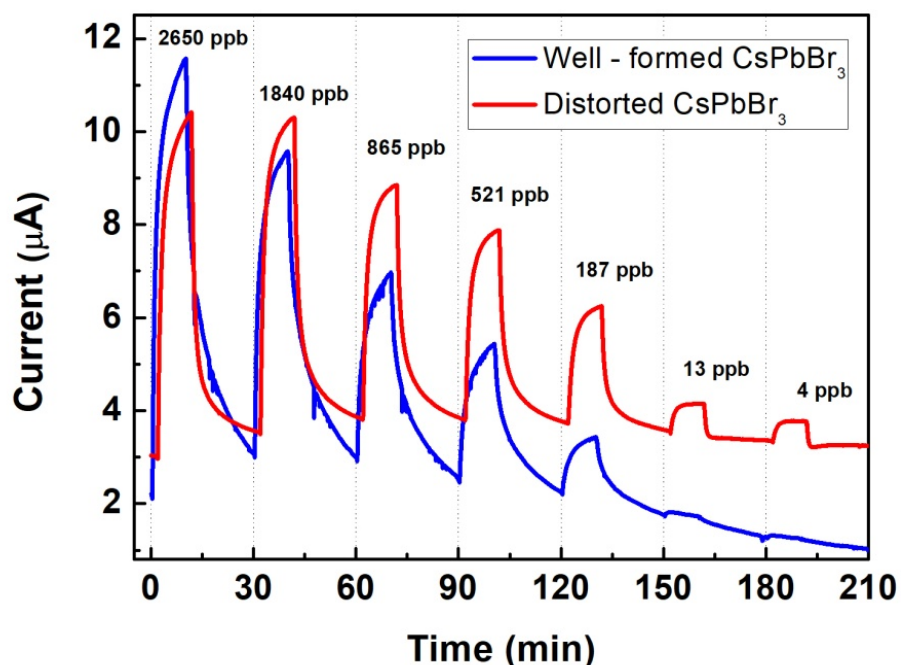


Figure 4.15 Comparison of electrical responses of al-inorganic lead halide well-formed and distorted nanocubes as a function of time upon different ozone concentrations.

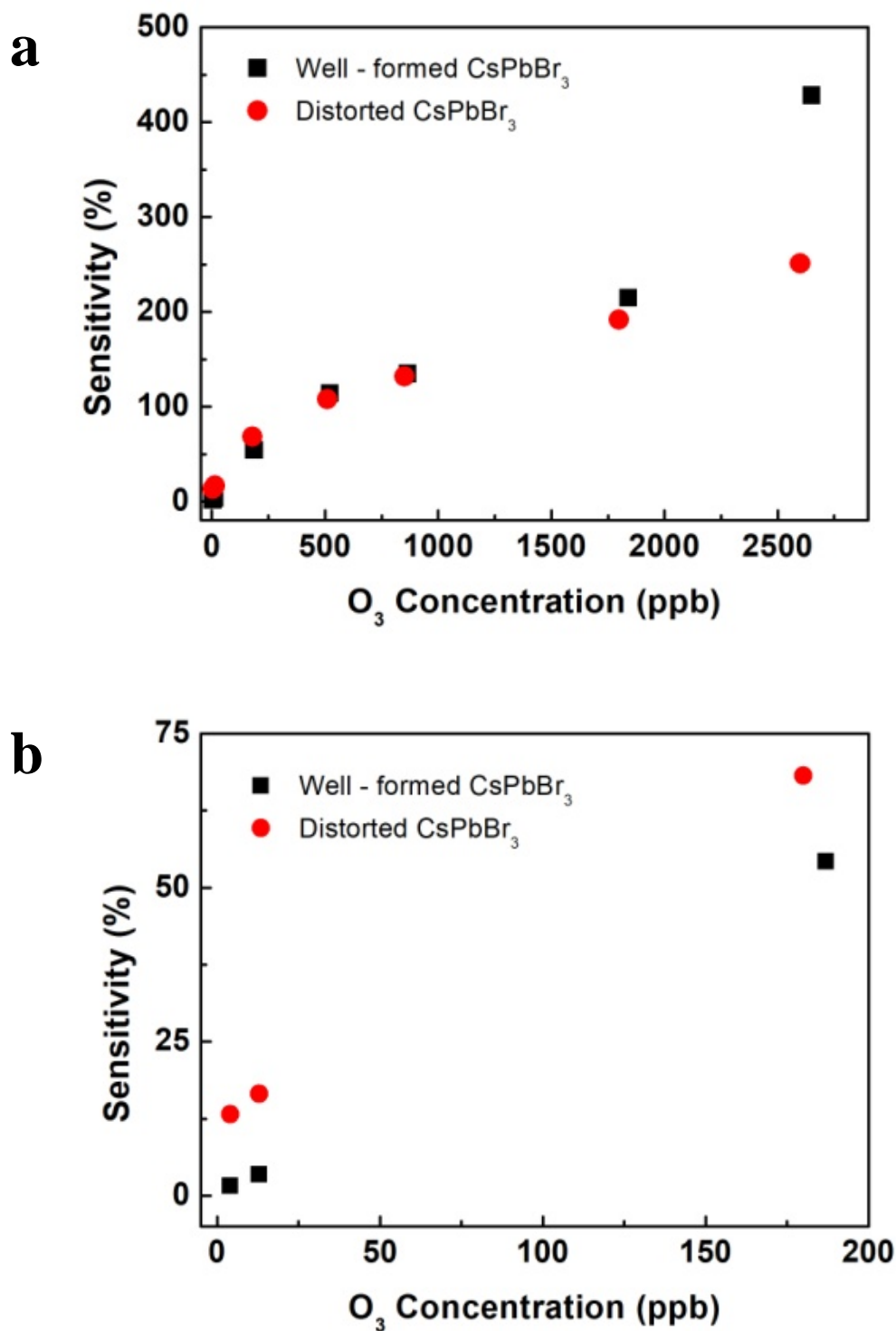


Figure 4.16 Sensitivity of well-formed and distorted nanocubes as a function of ozone concentrations

Figure 4.17 demonstrates the response and recovery times of both sensors as function of ozone concentration. It can be observed that the distorted sensing material responds faster in the presence of ozone gas compared with the well-formed nanocubes.

Additionally, the values of recovery time of the well-formed CsPbBr₃ sensor is almost three times higher than those measured for distorted CsPbBr₃ sensor.

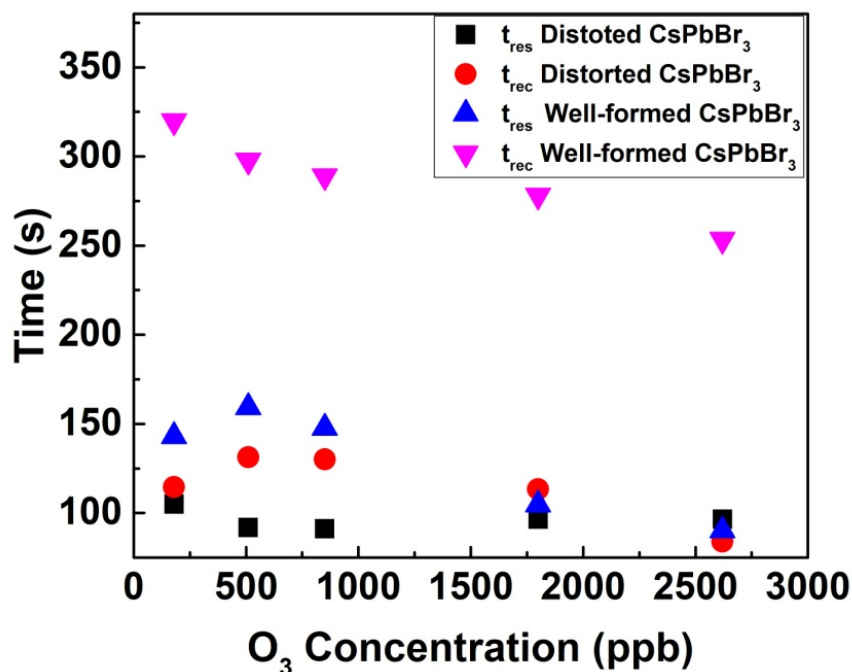


Figure 4.17 Comparison of response and recovery times of well-defined and distorted nanocubes as function of ozone concentration.

In addition, both sensing elements were further compared with other semiconducting materials reported in the literature for ozone sensing (Figure 4.18). It can be observed that distorted CsPbBr₃ nanocubes can detect the lowest ozone concentration at room temperature working conditions, exhibiting the highest sensitivity among the other sensing materials. It is also noteworthy that the sensitivity and durability of both CsPbBr₃ sensing elements are by far better than the hybrid organic-inorganic metal halide perovskite sensing film, which is the only lead halide perovskite material tested for O₃ sensing to date.⁵⁵

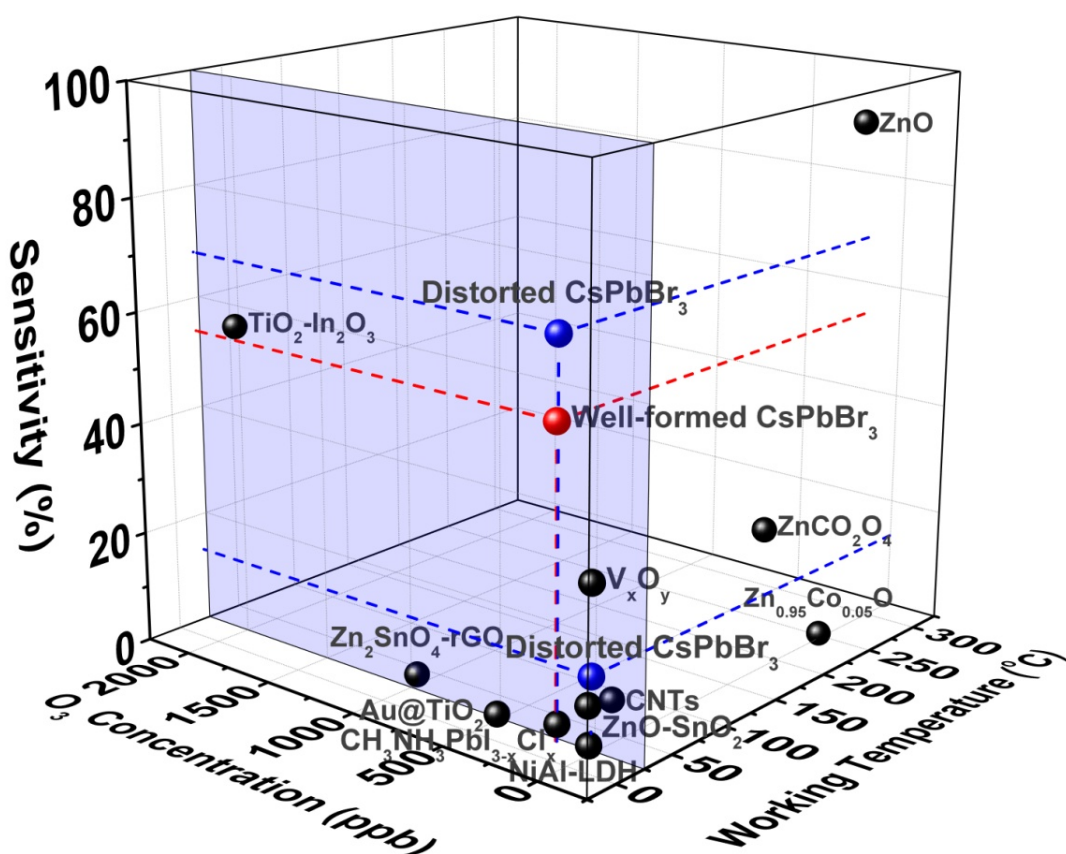


Figure 4.19 Sensitivity as function of O₃ concentration and working temperature for sensing elements reported in the literature.

4.3 Sensing Mechanism

The sensing behavior of CsPbBr₃ and distorted CsPbBr₃ nanocubes can be explained by Wolkenstein model.⁵⁶ According to this model, localized electronic states are created by adsorbed species. These states act as traps for electrons or holes depending on their nature. Particularly, when the sensor is exposed to air, neutral oxygen molecules are adsorbed on perovskite surface where they attract electrons from the valence band. Hence, oxygen molecules become partially ionized into O₂⁻, O⁻ and O²⁻. Due to the reduction of the number of electrons, a layer of holes covers the surface of the perovskite (Figure 4.20a). When the sensor is exposed to ozone gas, ozone molecules are adsorbed on the nanocube surface, increasing the number of holes in CsPbBr₃ shell lattice (Figure 4.20b). This current increase, caused by the increased electron trapping from the valence band, is typical behavior of a p-type semiconductor.⁵⁷

Since adsorption is a surface phenomenon, high surface-to-volume ratio leads to high adsorption. As shown in Figure 3.5, the edges of the distorted CsPbBr₃ nanocubes are slightly deformed resulting to an increase of their surface area. Moreover, distorted nanocubes are quite smaller than well-formed nanocubes which means that a greater

portion of atoms are found at the particle surface compared to those inside. Therefore, they exhibit higher surface-to-volume ratio than well-formed CsPbBr₃ nanocubes, explaining the higher sensitivity of the sensor.

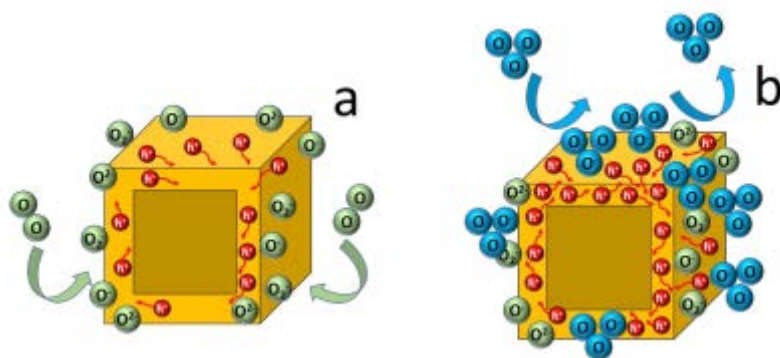


Figure 4.20 Schematic representation of the ozone sensing mechanism in ambient conditions (a) and after ozone exposure (b).

4.4 CsPbBr₃ Nanocubes for hydrogen gas sensing

a) Sensing properties of distorted CsPbBr₃ nanocubes

Considering the enhanced sensitivity of distorted CsPbBr₃ nanocubes compared to the well-formed one as ozone sensing material, their ability to detect hydrogen was also investigated by electrical measurements at room temperature with nitrogen as gas carrier for sensor's recovery. The sample was placed into the gas chamber and in the presence of nitrogen gas the initial current value was measured to be approximately 1 μ A.

The sensing performance of the sample was studied under different H₂ concentrations ranging from 100ppm to 1ppm. The electrical response of the sensor for all tested concentrations as a function of time is depicted on Figure 4.21a. Initially, the sensor was exposed to hydrogen gas with concentration of 100ppm for 3.5min, resulting to an immediate increase of the current intensity. Then, the recovery of the sample was followed by the replacement of hydrogen gas with pure nitrogen for 5min. The same procedure was repeated for all hydrogen concentrations and similar behavior was observed. Figure 4.22 demonstrates the evolution of minimum and maximum current values as a function of time. It is noticed that I_{\min} is quite stable as the concentration decreases, while I_{\max} increases upon increasing H₂ concentrations.

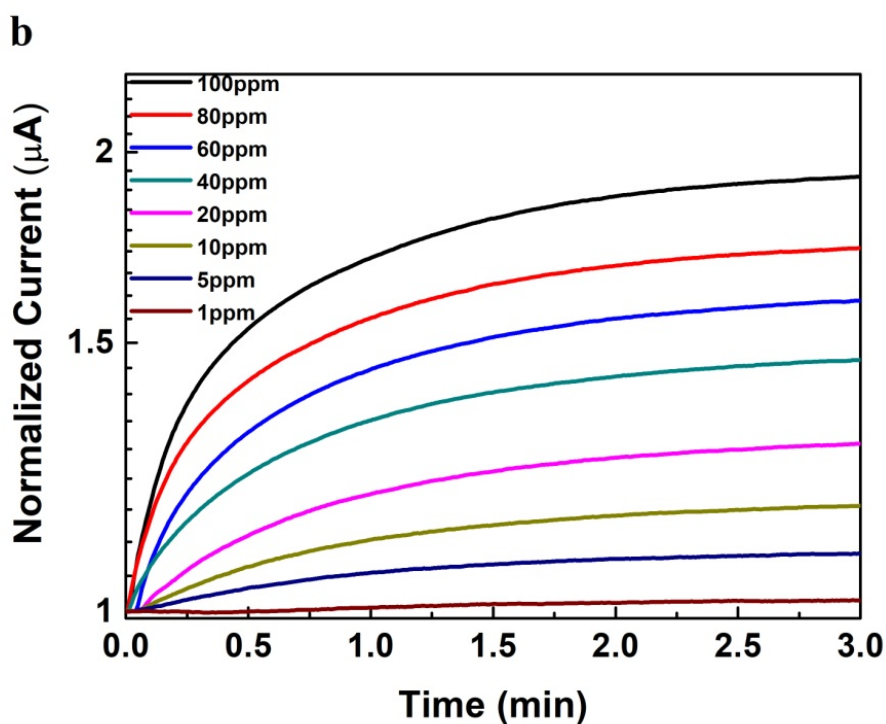
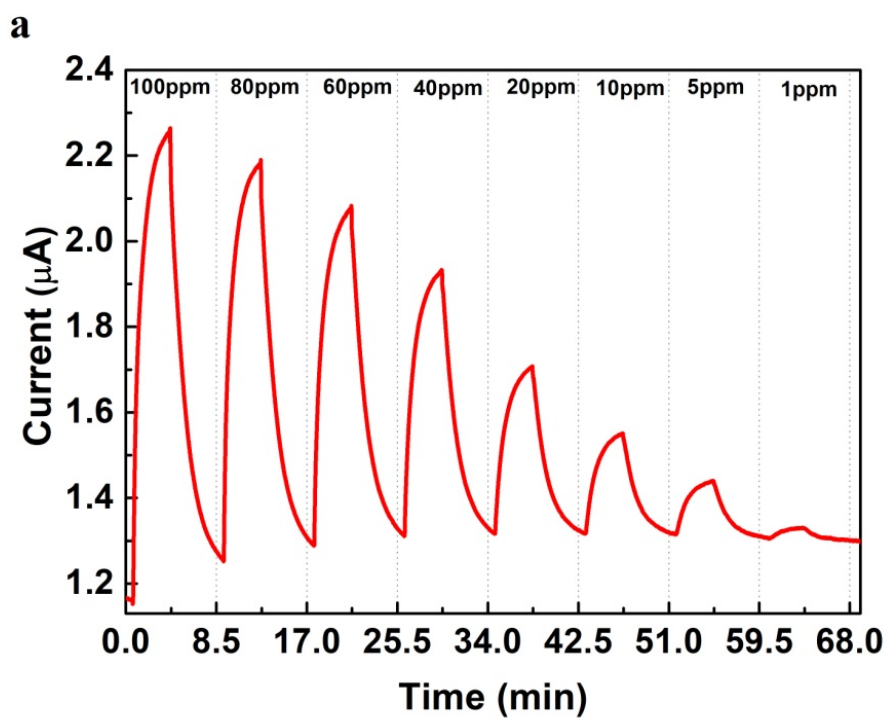


Figure 4.21 Electrical response of all-inorganic perovskite distorted nanocubes (a) and normalized exponential decay curves (b) as a function of time under different concentrations ranging from 100 ppm to 1 ppm.

In addition, the normalized exponential decay curves as a function of time during the hydrogen treatment are well-separated, even between 5ppm and 1ppm (Figure 4.21b). The well-distinguished curves reveal the sensor's high ability to resolve extremely

low hydrogen concentrations, with sensitivity increasing from 1.5% for 1ppm to almost 94% for 100ppm (Figure 4.22). Figure 4.23 illustrates the position of distorted CsPbBr₃ as sensing element among other semiconducting materials for hydrogen sensing. It can be observed that distorted CsPbBr₃ nanocubes exhibit the highest sensitivity (1.5%) and can detect the lowest H₂ concentration (1ppm) at room temperature working conditions. Notably, the sensitivity of the sensor at 5ppm is almost 10 times higher than the sensitivity at 1ppm.

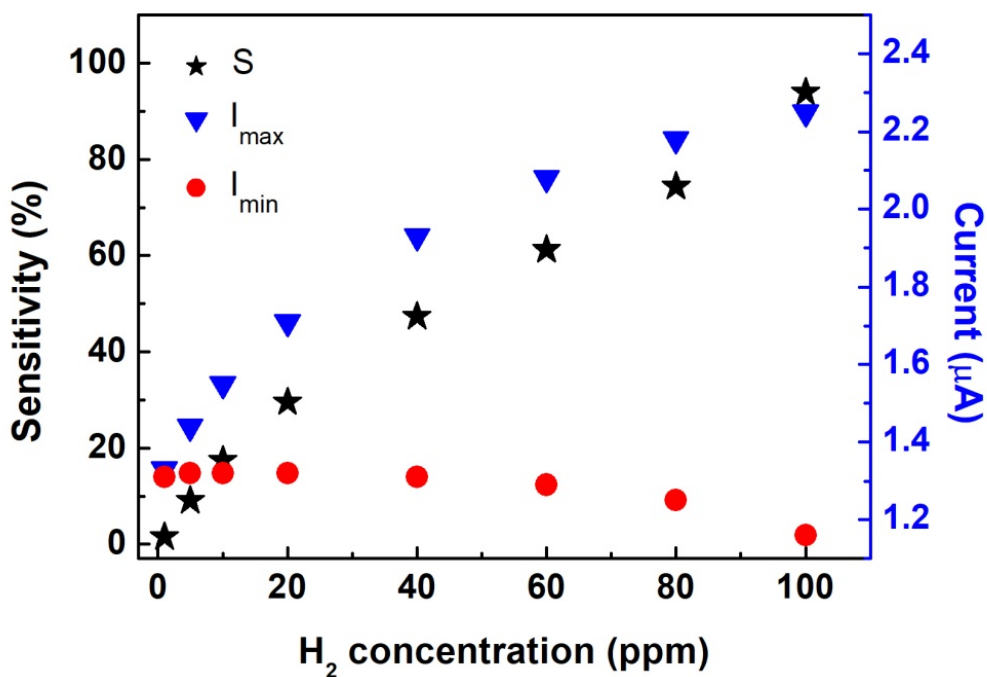


Figure 4.22 Sensitivity of H₂ sensor as a function of gas concentration

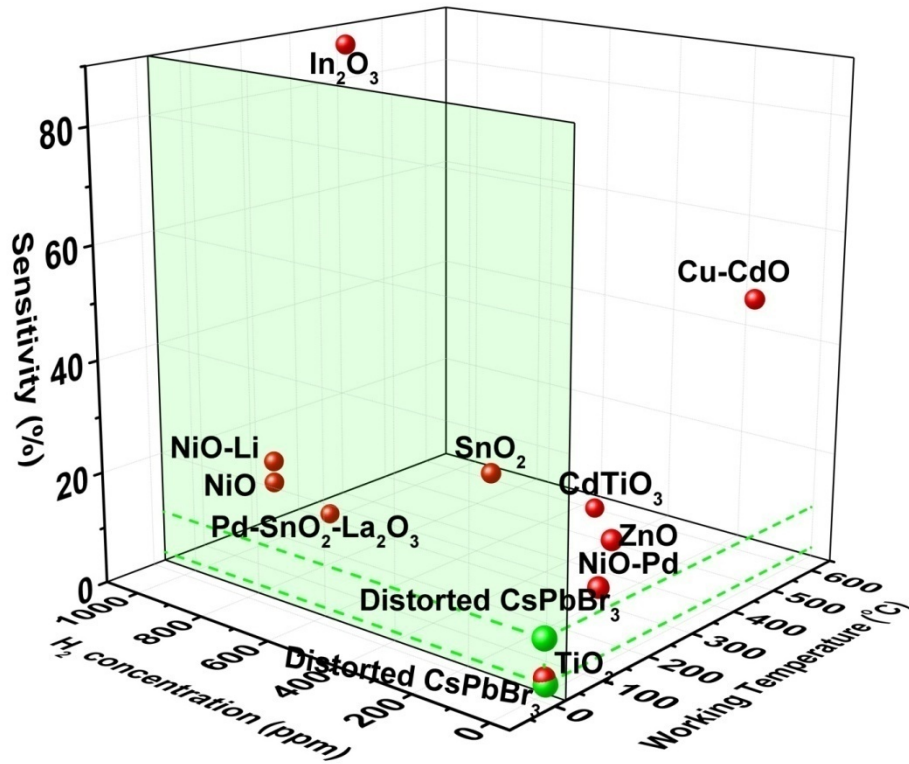


Figure 4.23 Sensitivity as function of H₂ concentration and working temperature of distorted CsPbBr₃ nanocubes and other semiconducting materials.^{58, 59, 60}

The sensor's quality was further characterized by the response and recovery times. Figure 4.24 presents the evolution of response and recovery times as a function of hydrogen concentration. In particular, t_{res} and t_{rec} values remain almost unchanged as hydrogen concentration increases with values between 43s to 75s, and 74s to 91s, respectively.

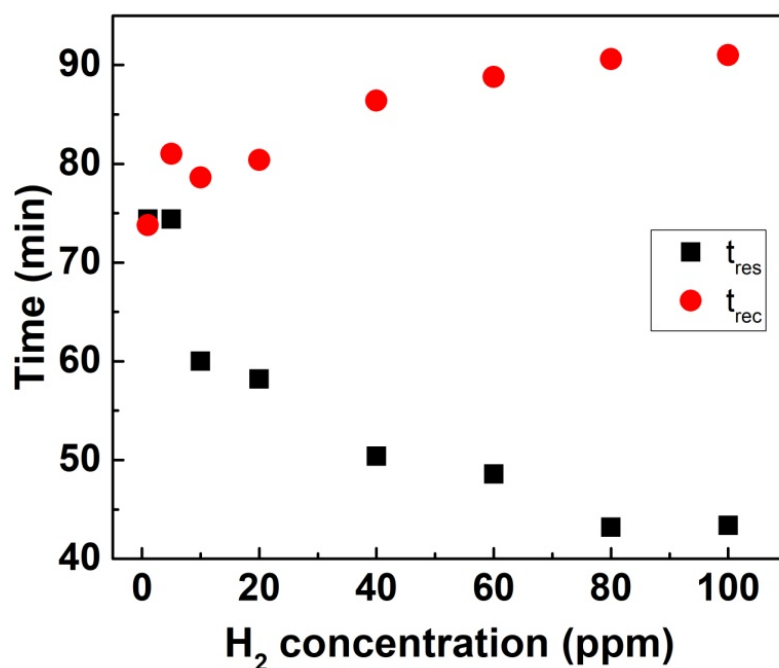


Figure 4.24 Response and recovery times as a function of H₂ concentration.

b) Stability of hydrogen sensor

A common demand in sensor technology is the ability to detect and monitor hydrogen at the lowest response time. However, stability and repeatability are two essential parameters that characterize the quality of a gas sensor. The repeatability of the sample was investigated during a series of H₂/N₂ switching cycles (Figure 4.25). It was observed that in the presence of H₂, the induced current was increasing, while in its absence current was decreasing, as expected. However, it is noted that the sensor was not fully recovered as the current did not reverse to its initial value, possibly due to adsorbed hydrogen molecules. Notably, at the end of the sensing process, distorted CsPbBr₃ nanocubes appear to retain their initial shape and morphology (Figure 4.26).

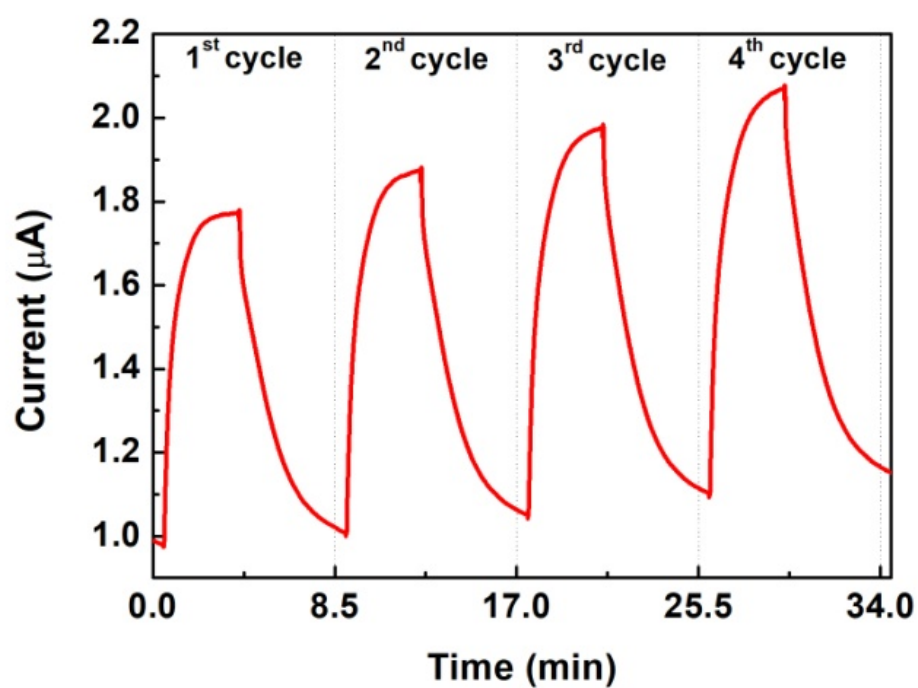


Figure 4.25 Electrical response of H₂ sensor upon four H₂/N₂ cycles as a function of time (a). SEM image of distorted CsPbBr₃ nanocubes at the end of the sensing process (b).

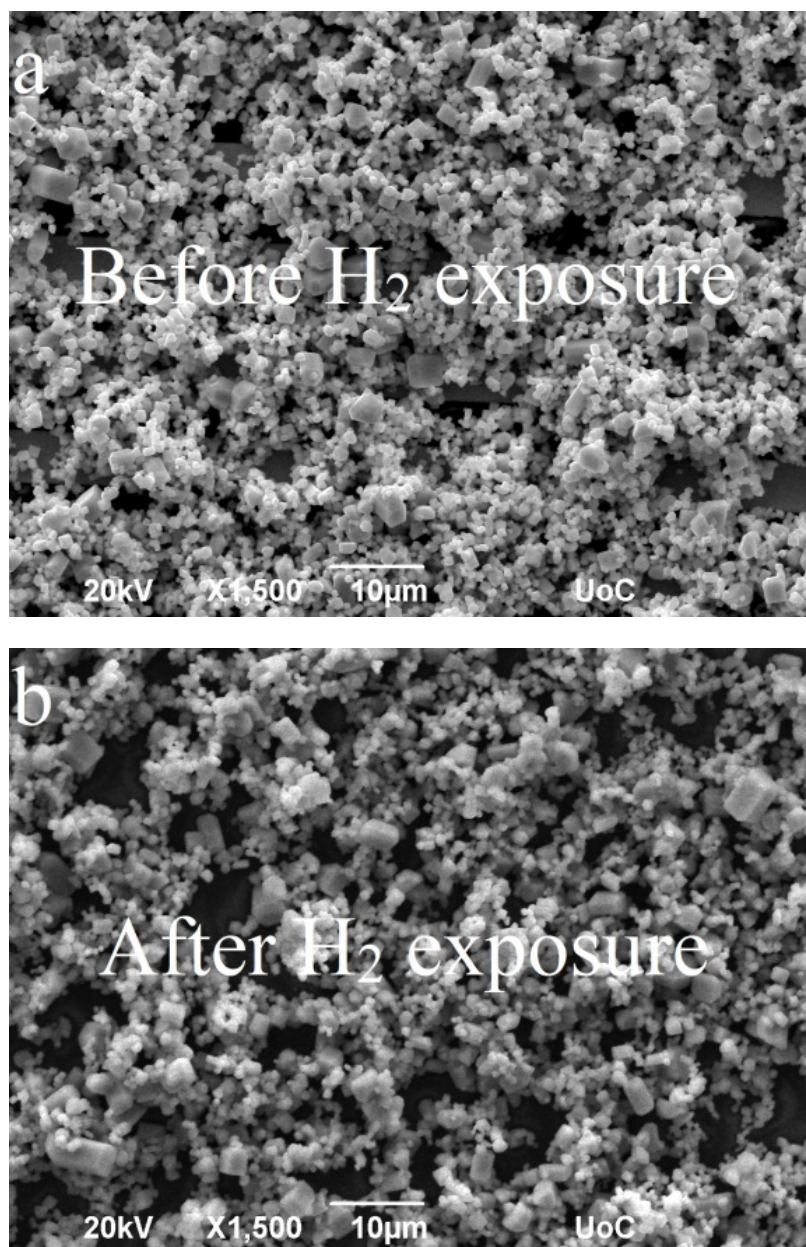


Figure 4.26 SEM images of distorted all-inorganic perovskites before (a) and after (b) H₂ exposure.

4.5 Sensing mechanism

The sensing mechanism of hydrogen is different to the previous reported for ozone, since hydrogen is known as a reducing agent while oxygen is an oxidizing agent and in both sensors the current intensity increases in the gaseous ambient.

Solution-processed cesium lead halide NCs are in great demand due to their high resistivity towards defect formation. However, those NCs are not totally free from defects. In particular, studies have shown that halogen vacancy is the most abundant defect in such NCs.⁶¹ Halogen vacancies act as major electron traps or recombination centers and mostly appear on the surface of NCs.⁶²

Consequently, the proposed mechanism is based on trap healing. Hydrogen molecules are adsorbed onto the perovskite surface. Since hydrogen molecule is the smallest size molecule that exists, it is the one which diffuses the most easily in materials. Hence H molecules are diffused inside the perovskite crystal and fill bromide vacancies which are intrinsically present in the crystal. Since bromide vacancies act as charge (electron) traps, their decreased number in presence of hydrogen translates into a higher number of charges (holes) available for electrical transport.⁶³

CHAPTER 5: CONCLUSIONS

In conclusion, ligand-free all-inorganic lead halide perovskite NCs have been prepared via a facile cost-effective solution-based method in both protective atmosphere and ambient conditions. Both samples exhibited a direct band gap with energy $E_g = 2.28 \text{ eV}$. In the first case, well-crystalline CsPbBr₃ nanocubes with sharp edges were formed directly on the substrate and were used as sensing element for ozone sensing application. The sensor exhibited high sensing ability within a wide range of O₃ concentrations, with sensitivity 54% at 187ppb which, according to the literature, is the highest reported among other metal oxides and metal halide perovskite materials to date. In addition, the well-formed CsPbBr₃ sensor was fully reversible after the response-recovery process under high O₃ concentrations proving its significant repeatability. Moreover, an advantage of this sensor is its ability to operate at room temperature without the need of external stimuli.

Following the fabrication of well-formed CsPbBr₃ nanocubes, distorted CsPbBr₃ nanocubes with deformed edges were prepared under ambient conditions. The main advantage of this technique is its simplicity and its low-cost fabrication process. Initially, this method was used for the preparation of an ultrasensitive ozone sensor. The sensor was self-powered and could operate at room temperature. In addition, its significantly higher sensitivity (13% at 4ppb) than those reported in the literature, its excellent repeatability under high O₃ concentrations and its fast response could be a breakthrough in the development of gas sensing applications.

Finally, the enhanced sensitivity as well as the simplicity of the preparation method made distorted CsPbBr₃ nanocubes a good candidate for more sensing applications. Hence, distorted all-inorganic lead halide perovskites were used as sensing elements for hydrogen gas sensing application. The sensor was able to detect fast extremely low hydrogen concentrations, with sensitivity ranging from 1.5% at 1ppm H₂ concentration to 94% at 100ppm. Moreover, its sensing ability is the highest among other metal oxides reported in the literature at room-operating temperature, providing new opportunities in sensing technology.

The present work is the first that demonstrates the application of ligand-free all-inorganic metal halide perovskite nanostructures as ozone and hydrogen sensing elements with great stability and durability. The results are very promising and could offer possibilities for new low-cost gas sensing applications with advanced features.

References

- 1 Ibrahim Khan, Khalid Saeed, and Idrees Khan, "Nanoparticles: Properties, Applications and Toxicities," *Arabian Journal of Chemistry*, May 2017, S1878535217300990, <https://doi.org/10.1016/j.arabjc.2017.05.011>.
- 2 Andrew M. Smith and Shuming Nie, "Semiconductor Nanocrystals: Structure, Properties, and Band Gap Engineering," *Accounts of Chemical Research* 43, no. 2 (February 16, 2010): 190–200, <https://doi.org/10.1021/ar9001069>.
- 3 Yasitha L. Hewakuruppu et al., "Plasmonic 'Pump-Probe' Method to Study Semi-Transparent Nanofluids," *Applied Optics* 52, no. 24 (August 20, 2013): 6041, <https://doi.org/10.1364/AO.52.006041>.
- 4 Mahmoud Nasrollahzadeh et al., "Types of Nanostructures," in *Interface Science and Technology*, vol. 28 (Elsevier, 2019), 29–80, <https://doi.org/10.1016/B978-0-12-813586-0.00002-X>.
- 5 Nikolai Khlebtsov and Lev Dykman, "Plasmonic Nanoparticles: Fabrication, Optical Properties, and Biomedical Applications," in *Handbook of Photonics for Biomedical Science*, ed. Valery Tuchin, vol. 20102371 (CRC Press, 2010), 37–85, <https://doi.org/10.1201/9781439806296-c2>.
- 6 Rizwan Khan et al., "Nanoparticles in Relation to Peptide and Protein Aggregation," *International Journal of Nanomedicine*, February 2014, 899, <https://doi.org/10.2147/IJN.S54171>.
- 7 Frank Alexis et al., "Factors Affecting the Clearance and Biodistribution of Polymeric Nanoparticles," *Molecular Pharmaceutics* 5, no. 4 (August 2008): 505–15, <https://doi.org/10.1021/mp800051m>.
- 8 Prashant K. Jain et al., "Au Nanoparticles Target Cancer," *Nano Today*, February 2007, vol. 2(1), 18–29, [https://doi.org/10.1016/S1748-0132\(07\)70016-6](https://doi.org/10.1016/S1748-0132(07)70016-6).
- 9 Zhaoning Song et al., "Pathways toward High-Performance Perovskite Solar Cells: Review of Recent Advances in Organo-Metal Halide Perovskites for Photovoltaic Applications," *Journal of Photonics for Energy* 6, no. 2 (April 15, 2016): 022001, <https://doi.org/10.1117/1.JPE.6.022001>.
- 10 Feng Zhang et al., "Brightly Luminescent and Color-Tunable Colloidal $\text{CH}_3\text{NH}_3\text{PbX}_3$ (X = Br, I, Cl) Quantum Dots: Potential Alternatives for Display Technology," *ACS Nano* 9, no. 4 (April 28, 2015): 4533–42, <https://doi.org/10.1021/acsnano.5b01154>.
- 11 Jia Liang et al., "All-Inorganic Perovskite Solar Cells," *Journal of the American Chemical Society* 138, no. 49 (December 14, 2016): 15829–32, <https://doi.org/10.1021/jacs.6b10227>.
- 12 Natalia Yantara et al., "Inorganic Halide Perovskites for Efficient Light-Emitting Diodes," *The Journal of Physical Chemistry Letters* 6, no. 21 (November 5, 2015): 4360–64, <https://doi.org/10.1021/acs.jpcllett.5b02011>.
- 13 Samuel W. Eaton et al., "Lasing in Robust Cesium Lead Halide Perovskite Nanowires," *Proceedings of the National Academy of Sciences* 113, no. 8 (February 23, 2016): 1993–98, <https://doi.org/10.1073/pnas.1600789113>.
- 14 Constantinos C. Stoumpos et al., "Crystal Growth of the Perovskite Semiconductor CsPbBr_3 : A New Material for High-Energy Radiation Detection," *Crystal Growth & Design* 13, no. 7 (July 3, 2013): 2722–27, <https://doi.org/10.1021/cg400645t>.

-
- 15 Sai Bai, Zhongcheng Yuan, and Feng Gao, "Colloidal Metal Halide Perovskite Nanocrystals: Synthesis, Characterization, and Applications," *Journal of Materials Chemistry C* 4, no. 18 (2016): 3898–3904, <https://doi.org/10.1039/C5TC04116C>.
- 16 Javad Shamsi et al., "Metal Halide Perovskite Nanocrystals: Synthesis, Post-Synthesis Modifications, and Their Optical Properties," *Chemical Reviews* 119, no. 5 (March 13, 2019): 3296–3348, <https://doi.org/10.1021/acs.chemrev.8b00644>.
- 17 M. Ahsan Zeb and Hae-Young Kee, "Interplay between Spin-Orbit Coupling and Hubbard Interaction in SrIrO₃ and Related Pbnm Perovskite Oxides," *Physical Review B* 86, no. 8 (August 31, 2012): 085149, <https://doi.org/10.1103/PhysRevB.86.085149>.
- 18 Ibrahim Dursun et al., "CsPb₂Br₅ Single Crystals: Synthesis and Characterization," *ChemSusChem* 10, no. 19 (October 9, 2017): 3746–49, <https://doi.org/10.1002/cssc.201701131>.
- 19 Kun-Hua Wang et al., "Large-Scale Synthesis of Highly Luminescent Perovskite-Related CsPb₂Br₅ Nanoplatelets and Their Fast Anion Exchange," *Angewandte Chemie International Edition* 55, no. 29 (July 11, 2016): 8328–32, <https://doi.org/10.1002/anie.201602787>.
- 20 Chenkun Zhou et al., "Low Dimensional Metal Halide Perovskites and Hybrids," *Materials Science and Engineering: R: Reports* 137 (July 2019): 38–65, <https://doi.org/10.1016/j.mser.2018.12.001>.
- 21 <https://www.nrel.gov/pv/cell-efficiency.html>.
- 22 Qiao Zhang and Yadong Yin, "All-Inorganic Metal Halide Perovskite Nanocrystals: Opportunities and Challenges," *ACS Central Science* 4, no. 6 (June 27, 2018): 668–79, <https://doi.org/10.1021/acscentsci.8b00201>.
- 23 Zhaohua Zhu et al., "Metal halide perovskites: stability and sensing-ability," *Journal of Materials Chemistry C*, (September 2018): 1–18, <https://doi.org/10.1039/x0xx00000x>.
- 24 Muhammad Aamir et al., "Cesium Lead Halide Perovskite Nanostructures: Tunable Morphology and Halide Composition," *The Chemical Record* 18, no. 2 (February 2018): 230–38, <https://doi.org/10.1002/tcr.201700034>.
- 25 Loredana Protesescu et al., "Nanocrystals of Cesium Lead Halide Perovskites (CsPbX₃, X = Cl, Br, and I): Novel Optoelectronic Materials Showing Bright Emission with Wide Color Gamut," *Nano Letters* 15, no. 6 (June 10, 2015): 3692–96, <https://doi.org/10.1021/nl5048779>.
- 26 Xiaoming Li et al., "All Inorganic Halide Perovskites Nanosystem: Synthesis, Structural Features, Optical Properties and Optoelectronic Applications," *Small* 13, no. 9 (March 2017): 1603996, <https://doi.org/10.1002/sml.201603996>.
- 27 A. Kostopoulou, E. Kymakis, and E. Stratakis, "Perovskite Nanostructures for Photovoltaic and Energy Storage Devices," *Journal of Materials Chemistry A* 6, no. 21 (2018): 9765–98, <https://doi.org/10.1039/C8TA01964A>.
- 28 R. F. Egerton, *Physical Principles of Electron Microscopy: An Introduction to TEM, SEM, and AEM* (New York, NY: Springer, 2005).
- 29 Michael Walock, "Nanocomposite Coatings Based on Quaternary Metalnitrogen," n.d., 211.
- 30 J. Garc'ia Sol'e, L.E. Baus'a and D. Jaque, "An Introduction to the Optical Spectroscopy of Inorganic Solids," (England, John Wiley & Sons Ltd, 2005)

-
- 31 Sun Jiulong, "Development of inorganic-organic hybrid materials for waste water treatment," n.d., 264.
- 32 Yoshio Waseda, Eiichiro Matsubara, and Kozo Shinoda, X-Ray Diffraction Crystallography: Introduction, Examples and Solved Problems (Heidelberg [Germany] ; New York: Springer, 2011)
- 33 Hideo Toraya, "Introduction to X-Ray analysis using the diffraction method," Rigaku Journal 32 no.2 (2016) , 35-43
- 34 <http://www.globalsino.com/EM/page3882.html>
- 35 Xiaoyu Zhang et al., "Water-Assisted Size and Shape Control of CsPbBr₃ Perovskite Nanocrystals," *Angewandte Chemie International Edition* 57, no. 13 (March 19, 2018): 3337–42, <https://doi.org/10.1002/anie.201710869>.
- 36 Bekir Turedi et al., "Water-Induced Dimensionality Reduction in Metal-Halide Perovskites," *The Journal of Physical Chemistry C* 122, no. 25 (June 28, 2018): 14128–34, <https://doi.org/10.1021/acs.jpcc.8b01343>.
- 37 Tetsuro Seiyama et al., "A New Detector for Gaseous Components Using Semiconductive Thin Films.," *Analytical Chemistry* 34, no. 11 (October 1962): 1502–3, <https://doi.org/10.1021/ac60191a001>.
- 38 P. Å. Öberg, Tatsuo Togawa, and Francis A. Spelman, eds., "Front Matter," in *Sensors in Medicine and Health Care* (Weinheim, FRG: Wiley-VCH Verlag GmbH & Co. KGaA, 2004), i–XXIV, <https://doi.org/10.1002/3527601414.fmatter>.
- 39 Ana M. Ruiz et al., "Effects of Various Metal Additives on the Gas Sensing Performances of TiO₂ Nanocrystals Obtained from Hydrothermal Treatments," *Sensors and Actuators B: Chemical* 108, no. 1–2 (July 2005): 34–40, <https://doi.org/10.1016/j.snb.2004.09.045>.
- 40 Nicholas P. Cheremisinoff, ed., "Faculative Ponds," in *Pollution Control Handbook for Oil and Gas Engineering* (Hoboken, NJ, USA: John Wiley & Sons, Inc., 2016), 467–72, <https://doi.org/10.1002/9781119117896.ch37>.
- 41 Masanori Ando, Vasudevanpillai Biju, and Yasushi Shigeri, "Development of Technologies for Sensing Ozone in Ambient Air," *Analytical Sciences* 34, no. 3 (2018): 263–71, <https://doi.org/10.2116/analsci.34.263>.
- 42 Dongwook Lee et al., "A Novel Optical Ozone Sensor Based on Purely Organic Phosphor," *ACS Applied Materials & Interfaces* 7, no. 5 (February 11, 2015): 2993–97, <https://doi.org/10.1021/am5087165>.
- 43 G. Korotcenkov, V. Brinzari, and B. K. Cho, "In₂O₃ - and SnO₂ -Based Thin Film Ozone Sensors: Fundamentals," *Journal of Sensors* 2016 (2016): 1–31, <https://doi.org/10.1155/2016/3816094>.
- 44 Xiaobing Pang et al., "Electrochemical Ozone Sensors: A Miniaturised Alternative for Ozone Measurements in Laboratory Experiments and Air-Quality Monitoring," *Sensors and Actuators B: Chemical* 240 (March 2017): 829–37, <https://doi.org/10.1016/j.snb.2016.09.020>.
- 45 G. Korotcenkov and B.K. Cho, "Ozone Measuring: What Can Limit Application of SnO₂-Based Conductometric Gas Sensors?," *Sensors and Actuators B: Chemical* 161, no. 1 (January 2012): 28–44, <https://doi.org/10.1016/j.snb.2011.12.003>.
- 46 G. Korotcenkov, V. Brinzari, and B. K. Cho, "In₂O₃ - and SnO₂ -Based Ozone Sensors: Design and Characterization," *Critical Reviews in Solid State and Materials Sciences* 43, no. 2 (March 4, 2018): 83–132, <https://doi.org/10.1080/10408436.2017.1287661>.

-
- 47 Windholz, M., S. Budavari, L.Y. Stroumtsos, and M.N. Fertig, eds. 1976. P. 631 in the Merck Index: An Encyclopedia of Chemicals and Drugs, 9th Ed. Rahway, NJ: Merck.
- 48 T. Hübert et al., “Hydrogen Sensors – A Review,” *Sensors and Actuators B: Chemical* 157, no. 2 (October 2011): 329–52, <https://doi.org/10.1016/j.snb.2011.04.070>.
- 49 M. Kandyla et al., “Nanocomposite NiO:Pd Hydrogen Sensors with Sub-Ppm Detection Limit and Low Operating Temperature,” *Materials Letters* 119 (March 2014): 51–55, <https://doi.org/10.1016/j.matlet.2013.12.104>.
- 50 E T H Tan et al., “Gas Sensing Properties of Tin Oxide Nanostructures Synthesized via a Solid-State Reaction Method,” *Nanotechnology* 19, no. 25 (June 25, 2008): 255706, <https://doi.org/10.1088/0957-4484/19/25/255706>.
- 51 Fatemeh Moosavi et al., “Hydrogen Sensing Properties of Co-Doped ZnO Nanoparticles,” *Chemosensors* 6, no. 4 (December 5, 2018): 61, <https://doi.org/10.3390/chemosensors6040061>.
- 52 Chi Lu and Zhi Chen, “High-Temperature Resistive Hydrogen Sensor Based on Thin Nanoporous Rutile TiO₂ Film on Anodic Aluminum Oxide,” *Sensors and Actuators B: Chemical* 140, no. 1 (June 2009): 109–15, <https://doi.org/10.1016/j.snb.2009.04.004>.
- 53 Wan-Young Chung et al., “Preparation of Indium Oxide Thin Film by Spin-Coating Method and Its Gas-Sensing Properties,” *Sensors and Actuators B: Chemical* 46, no. 2 (February 1998): 139–45, [https://doi.org/10.1016/S0925-4005\(98\)00100-2](https://doi.org/10.1016/S0925-4005(98)00100-2).
- 54 S.J. Ippolito et al., “Hydrogen Sensing Characteristics of WO₃ Thin Film Conductometric Sensors Activated by Pt and Au Catalysts,” *Sensors and Actuators B: Chemical* 108, no. 1–2 (July 2005): 154–58, <https://doi.org/10.1016/j.snb.2004.11.092>.
- 55 George Kakavelakis et al., “Solution Processed CH₃NH₃PbI_{3-x}Cl_x Perovskite Based Self-Powered Ozone Sensing Element Operated at Room Temperature,” *ACS Sensors* 3, no. 1 (January 26, 2018): 135–42, <https://doi.org/10.1021/acssensors.7b00761>.
- 56 F. F. Vol'kenshteĭn, *Electronic Processes on Semiconductor Surfaces during Chemisorption* (New York: Consultants Bureau, 1991).
- 57 S. Thirumalairajan and Valmor R. Mastelaro, “A Novel Organic Pollutants Gas Sensing Material P-Type CuAlO₂ Microsphere Constituted of Nanoparticles for Environmental Remediation,” *Sensors and Actuators B: Chemical* 223 (February 2016): 138–48, <https://doi.org/10.1016/j.snb.2015.09.092>.
- 58 Ian M. Walton et al., “The Role of Atropisomers on the Photo-Reactivity and Fatigue of Diarylethene-Based Metal–Organic Frameworks,” *New Journal of Chemistry* 40, no. 1 (2016): 101–6, <https://doi.org/10.1039/C5NJ01718A>.
- 59 Xiaohong Xia et al., “A Hydrogen Sensor Based on Orientation Aligned TiO₂ Thin Films with Low Concentration Detecting Limit and Short Response Time,” *Sensors and Actuators B: Chemical* 234 (October 2016): 192–200, <https://doi.org/10.1016/j.snb.2016.04.110>.
- 60 I. Sta et al., “Hydrogen Sensing by Sol–Gel Grown NiO and NiO:Li Thin Films,” *Journal of Alloys and Compounds* 626 (March 2015): 87–92, <https://doi.org/10.1016/j.jallcom.2014.11.151>.

-
- 61 Sudipta Seth et al., “Tackling the Defects, Stability, and Photoluminescence of CsPbX₃ Perovskite Nanocrystals,” *ACS Energy Letters* 4, no. 7 (July 12, 2019): 1610–18, <https://doi.org/10.1021/acseenergylett.9b00849>.
- 62 Hongliang Shi and Mao-Hua Du, “Shallow Halogen Vacancies in Halide Optoelectronic Materials,” *Physical Review B* 90, no. 17 (November 5, 2014): 174103, <https://doi.org/10.1103/PhysRevB.90.174103>.
- 63 Marc-Antoine Stoeckel et al., “Reversible, Fast, and Wide-Range Oxygen Sensor Based on Nanostructured Organometal Halide Perovskite,” *Advanced Materials* 29, no. 38 (October 2017): 1702469, <https://doi.org/10.1002/adma.201702469>.